Environ. Sci. Technol. **2010,** *44,* 7814–7820

Natural Attenuation of Zinc Pollution in Smelter-Affected Soil

M. VESPA,[†] M. LANSON, AND A. MANCEAU*

Mineralogy & Environments Group, ISTerre, University Joseph Fourier and CNRS, 38041 Grenoble Cedex 9, France

Received May 11, 2010. Revised manuscript received August 25, 2010. Accepted September 1, 2010.

Previous synchrotron X-ray microprobe measurements of Zn speciation in contaminated and uncontaminated soils have identified phyllosilicate as the main sequestration phase. The emphasis now is focused on comparing the nature and properties of neoformed and geogenic phyllosilicate species to understand natural attenuation processes. Refined structural characterization of the two types of Zn-containing phyllosilicate in slightly basic smelter-affected agricultural soils were obtained using a so far unprecedented combination of X-ray microscopic techniques, including fluorescence (μ-XRF), absorption (μ-EXAFS), and diffraction (μ-XRD), and X-ray bulk-sensitive techniques, including powder and polarized EXAFS spectroscopy. The unpolluted and polluted species are both dioctahedral smectites, but the first which contains minor Zn (ca. 150 mg/kg) is aluminous and Fe-free, and the second, which contains several hundreds to a few thousands mg/kg Zn depending on the distance to the smelter and wind direction, is ferruginous with an average Fe/Al atomic ratio of 1.1 $\pm$ 0.5. The Zn^{2+} and Fe^{3+} in the neoformed smectite are derived from the weathering of ZnS, ZnO, FeS_2, and $ZnFe_2O_4$ particles from the smelter. These cations diffuse away from their particulate mineral sources and coprecipitate with Al and Si in the soil clay matrix. Zinc sequestration in the octahedral sheet of dioctahedral smectite is potentially irreversible, because this type of phyllosilicate is stable over a large pH range, and the neoformed species is analogous to the native species which formed over time during pedogenesis.

Introduction

In the past centuries, smelting activities throughout the world resulted in the release of large amounts of heavy metal(loid)s, including Cd, Pb, Zn, and As (*1*). Elevated concentrations of these elements can have strong adverse effects on soil ecological functions, such as reduced primary production and reduced nutrient cycling (*2, 3*). Although Zn is not considered as one of the most serious threats to living organisms, its labile pool is easily taken up by roots and translocated to the shoots, and excessive uptake generally correlates negatively with biomass production. Zinc can be also inaccessible in soil. Understanding its speciation in this less mobile pool at the atomic and molecular scale is critical to (i) developing a scientific basis for maintaining soil quality, (ii) predicting the time-evolution of metal mobility and bioavailability at contaminated sites (natural attenuation of pollution), and (iii) formulating effective remediation strategies.

Until recently, our knowledge of the speciation of Zn in contaminated sites was limited to characterizing well-crystallized phases, generally primary minerals from the source of pollution (ore, slag material). The advent of X-ray microprobes (*4*) made possible the identification of secondary forms, produced by the weathering of primary minerals, and chemical reactions of dissolved species with matrix constituents in contact with pore waters. Using micro X-ray fluorescence (μ-XRF) and extended X-ray absorption fine structure (μ-EXAFS) spectroscopy various authors have found that Zn entered the structure of phyllosilicate, layer double hydroxide (LDH), phyllomanganate, iron oxyhydroxide, carbonate, and was complexed to organics (*5*−*24*). Zinc can be incorporated and stabilized by a large number of secondary minerals, because its ionic radius (0.60 Å for tetrahedral Zn, 0.74 Å for octahedral Zn) is similar to those of the main cations present in soils, i.e. Al (0.53 Å), Fe (0.64 Å Fe^{3+}, 0.78 Å Fe^{2+}), and Mg (0.72 Å), and can be octahedral or tetrahedral (*16*).

Zinc generally is associated predominantly with phyllosilicate in contaminated soils, and this pool is considered to be mostly stable based on the widespread occurrence of Zn-containing clays in uncontaminated environments (*15*−*17*). In this study, we seek to know whether phyllosilicate species neoformed in smelter-affected soil can be differentiated from the native background species originally present in the soil matrix. In other words, do natural attenuation processes that convert Zn over time to less detrimental forms lead to a specific structure fingerprint in this type of soil? To address this question, a so far unprecedented combination of X-ray techniques, including μ-XRF, micro diffraction (μ-XRD), and powder-, polarized-, and micro EXAFS, were used and provided powerful synergy to scrutinize the local structural environment of Zn in neoformed and natural phyllosilicate.

Experimental Methods

Materials. The samples come from tilled pseudogley brown leached soils developed on Eocene sands and clays (pH ~8) in northern France near the city of Douai, 40 km south of Lille (*25*). The whole area has been contaminated by atmospheric deposition from a smelter in operation for over a century until its closure in 2003. The main primary minerals released from the metallurgical smelting process were pyromorphite ($Pb_5(PO_4)_3Cl$), sphalerite (ZnS), Zn-spinels ($Zn(Fe,Al,Cr)_2O_4$, i.e. franklinite, gahnite, chromite), and zincite (ZnO) (*6, 12, 14, 21*). A 40 km^2 area around the smelter was delimited, divided into 160 grids (one grid = 0.5 × 0.5 km^2), and analyzed for heavy metals concentrations (*25*). Total Zn concentrations in this area range from 115 to 2515 mg/kg in agricultural soils (mean = 450 ± 306) and are generally higher in woody habitat soils (mean = 885 ± 2512). Three sampling sites in agricultural lands were chosen at 0.5 km southeast from the smelter (A), 1.4 km northeast and downwind from the smelter (B), and at 3 km in the north−northeast direction under intermediate winds (C). Bulk and undisturbed samples were collected from the topsoils (0−15 cm depth) and subsoils or hard pans (35−50 cm depth) with total Zn concentrations of 1092, (Aa), 430 (Ba), and 287 (Ca) and 69 (Ab), 67(Bb), and 102 (Cb) mg/kg, respectively (Table S1). The concentrations in the subsoils are typical of the regional geochemical background (68 mg/kg (*25*)), whereas with several hundreds mg/kg Zn, the topsoils are clearly contaminated by the smelter. The sieved <2 mm fractions were used for powder EXAFS, and self-supporting

* Corresponding author phone: +33 4 76 63 5193; fax: +33 4 79 75 87 77; e-mail: Alain.Manceau@ujf-grenoble.fr.

[†] Present address: Institute for Transuranium Elements, Joint Research Centre, Postfach 2340, D-76125 Karlsruhe, Germany.

10.1021/es101567u

© 2010 American Chemical Society

Published on Web 09/20/2010

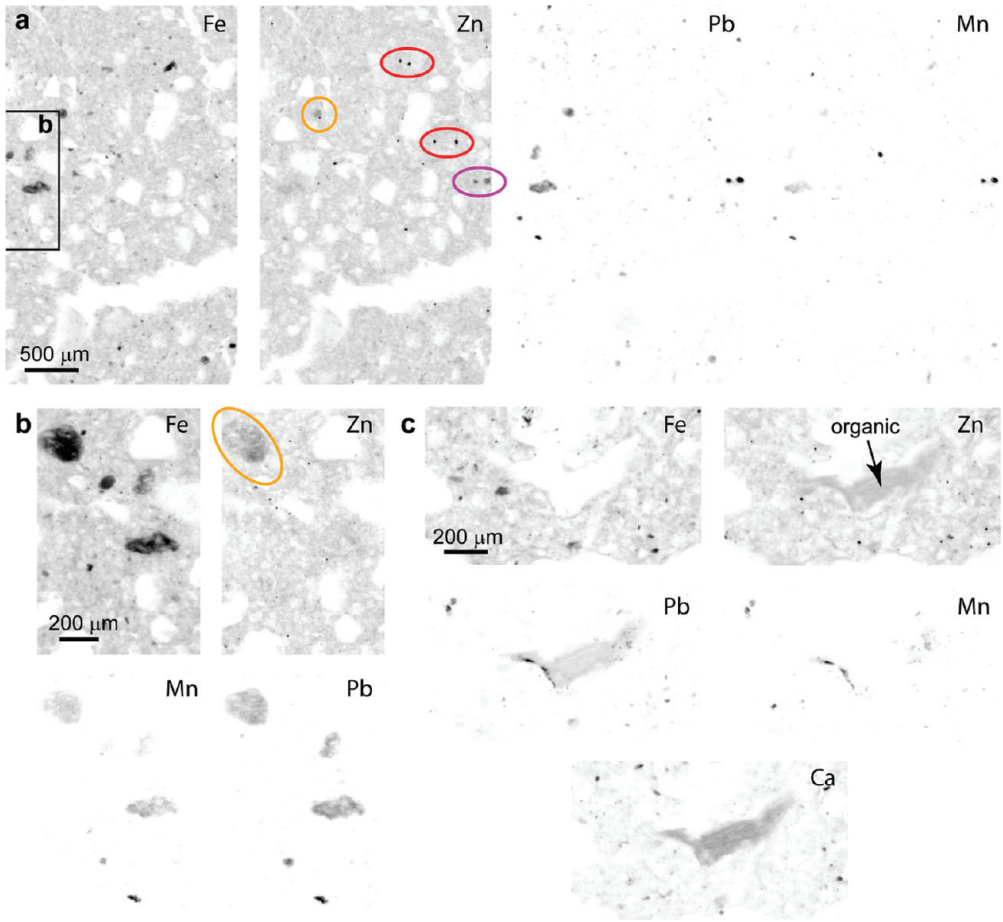

FIGURE 1. Representative micro X-ray fluorescence (μ-XRF) grayscale maps of Mn, Fe, Zn, and Pb in the topsoils. The ellipses highlight the correlations of Zn with Fe (light brown) and with Mn (purple), and the hot-spots (red) from primary grains (ZnS, ZnO, $ZnFe_2O_4$). (a) Coarse map at 10 × 10 μm^2 resolution. (b) Fine map at 7 × 7 μm^2 resolution of an enlarged region from (a). (c) Organic debris rich in Zn and Pb mapped at 5 × 5 μm^2 resolution. Its lower-left edge is coated with a Mn−Pb precipitate.

films were prepared for polarized-EXAFS (P-EXAFS) from the clay fractions (<2 μm). The concentrations of Zn in the clay fractions were 2550 (Aa), 1090 (Ba), 610 (Ca), 140 (Ab), 160 (Bb), and 160 (Cb) mg/kg. Cationic exchange measurements showed that less than 1% of total Zn was exchangeable or weakly bound in the <2 mm and <2 μm fractions. This pool is too minor to be discerned by EXAFS spectroscopy. The mineralogy of the clay fractions was characterized in the laboratory by XRD. The undisturbed samples were impregnated, abraded, and polished to 30 μm thickness, and the thin sections were peeled off from the glass support for micro X-ray fluorescence (μ-XRF) mapping and diffraction (μ-XRD) measurements.

Methods. Zn K-edge bulk and polarized EXAFS spectra were collected on the FAME beamline (BM30B) at the European Synchrotron Radiation Facility (ESRF) in Grenoble, France (*26*). The P-EXAFS spectra were collected at four angles: $\alpha = 10°, 35°, 55°, 80°$ (*27*). The $\alpha = 35°$ spectra from oriented films are identical to those from powder preparations (i.e., 'magic angle' (*28*)). Micro XRF, EXAFS, and XRD data were collected on beamline 10.3.2 at the Advanced Light Source (ALS) in Berkeley, USA (*29*). All data were analyzed using standard procedures described in the Supporting Information.

Results and Interpretations

Zn Speciation. Several regions in the thin sections of the three topsoils were examined by μ-XRD to inventory the dominant Zn species from the observed chemical associations and from the shape, size, and composition of the grains and aggregates in the clayey matrix. The μ-XRF maps shown in Figure 1 represent the variety of particle morphologies and compositions observed in the thin-section maps. Zinc was found everywhere in the ferruginous matrix. Its distribution contrasts with that of Pb, which is mostly in regions and particles enriched in Fe and/or Mn. Clearly, Pb has not fully permeated the whole fine matrix as Zn did. Some of the ferri-manganiferous areas enriched in Pb also contain Zn, but this association with Fe and Mn is less systematic for Zn than for Pb. Zn and Pb are coassociated also in organic debris, easily recognized by their higher Ca content and generally reticular structure at high resolution (Figure 1c).

Micro XRD on the Mn aggregates identified vernadite (turbostratic phyllomanganate) from the 100 and 110 reflections at 2.45 Å and 1.42 Å, respectively (Figure S1a). Micro EXAFS showed that Zn is tetrahedrally coordinated and sits atop vacancy sites of the Mn layers, as commonly observed in soils and sediments (*7, 15*) (Figure S1b). In Fe-rich areas, diffraction maxima matched those of goethite (Figure S1c), and the Zn-EXAFS spectrum was most similar to that of Zn-substituted goethite (Figure S1d). The μ-XRD pattern collected on the organic species (Figure S1e) showed reflection belonging only to the resin, suggesting that Zn is bound to a noncrystalline species. From the similarity between the μ-EXAFS spectra collected on the same region and Zn bound to carboxyl groups, it was concluded that this species is organic (Figure S1f).

Twenty-two spectra were recorded in the fine matrix of the topsoils. Most of them were statistically invariant or differed slightly in amplitude and detailed shape of some

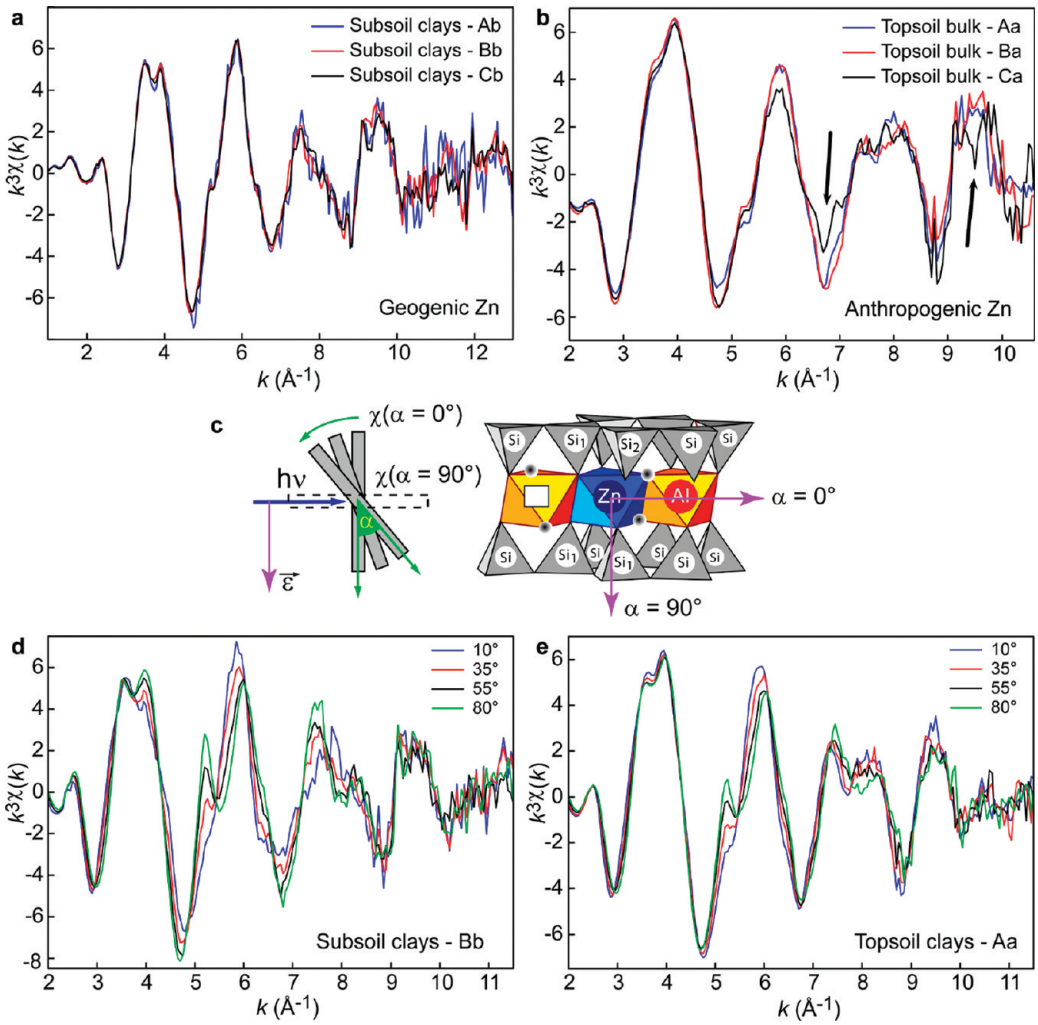

FIGURE 2. (a,b) Zn K-edge powder EXAFS spectra of the clay fractions from the subsoils (a) and the <2 mm bulk fraction from the topsoils (b). (c) Successive orientations of a clay film in the X-ray beam during P-EXAFS measurements. ε is the electric field (polarization) vector. Polyhedral representation of a Zn-containing dioctahedral phyllosilicate. The arrows indicate the α angles between the polarization vector and a clay layer. (d,e) Polarized EXAFS spectra for two clay films from the subsoil (d) and topsoil (e). Samples Aa and Bb were chosen for this analysis from the measurements of all clay films at α = 35°, because Aa was the richest in Zn and Bb had the highest Zn/Fe ratio (i.e., highest signal-to-noise ratio in (a)). The $k^3\chi_\alpha(k)$ data were regressed following the procedure described in ref *27*.

EXAFS features. They all exhibited a splitting of the first oscillation at $k \sim 3.7$ Å^{-1}, a shoulder at $k = 5.0-5.5$ Å^{-1}, and a line shape of the third oscillation that were observed previously for Zn and soil phyllosilicates (*14, 30*) (Figure S2). The Zn-LDH phase, which if present in soils and sediments is usually minor and easily transformed to phyllosilicate (*8, 9, 11, 13, 20, 31−33*), has a distinctive EXAFS signature from the μ-EXAFS spectra of the topsoils (SI). In summary, a total of four Zn species were identified through the combination of micro XRF, XRD, and EXAFS: phyllomanganate (vernadite), Fe oxyhydroxide (mostly goethite), organic, and phyllosilicate with some variation in the exact bonding environment of Zn. From μ-XRF, the last species seems predominant. However, the representativeness of the four species should be evaluated by upscaling from microscopic observations to the whole topsoil to know if what is found in the entire sample truly can be represented by one major and three minor species.

This question was addressed in two independent, yet complementary ways: by recording the bulk EXAFS spectra from the <2 mm fractions for the three topsoils and the polarized EXAFS spectra from their clay fractions (Figure 2). Three other clay films also were prepared from the subsoils to compare the bonding environment of Zn in the anthropogenic and geogenic phyllosilicate pools, and to determine if the neoformed and background species were the same in the three soils. The clay films were prepared from the <2 μm fractions extracted from about one kilogram of an homogenized field sampling of several kilograms, and so the data are representative of the average Zn speciation in the clayey matrix. Based on chemical analysis, the contributions of geogenic Zn in the topsoils Aa, Ba, and Ca are approximately 5%, 15%, and 26%, respectively (Table S1).

Dominant Speciation. Zinc has the same speciation in the clay fractions of the three subsoils, consistent with a geogenic origin for this species, and its EXAFS spectrum is analogous to that of a phyllosilicate (Figures 2a). The Zn/Fe ratios of the three unfractionated (i.e., < 2 mm) subsoils were too low to obtain good bulk data. However, chemical analysis suggests that the geogenic phyllosilicate species represents the main form of Zn in the hard pans (Table S1). Zinc has a similar average speciation in the entire topsoils Aa and Ba, but detectable local structural differences were observed in Ca (Figure 2b). The three bulk spectra have considerable similarities with the μ-EXAFS spectrum of the neoformed phyllosilicate species and with the P-EXAFS spectra of the clay fractions (Figures 2 and S2). Thus, size-fractionation did not modify or only marginally modified the initial form of

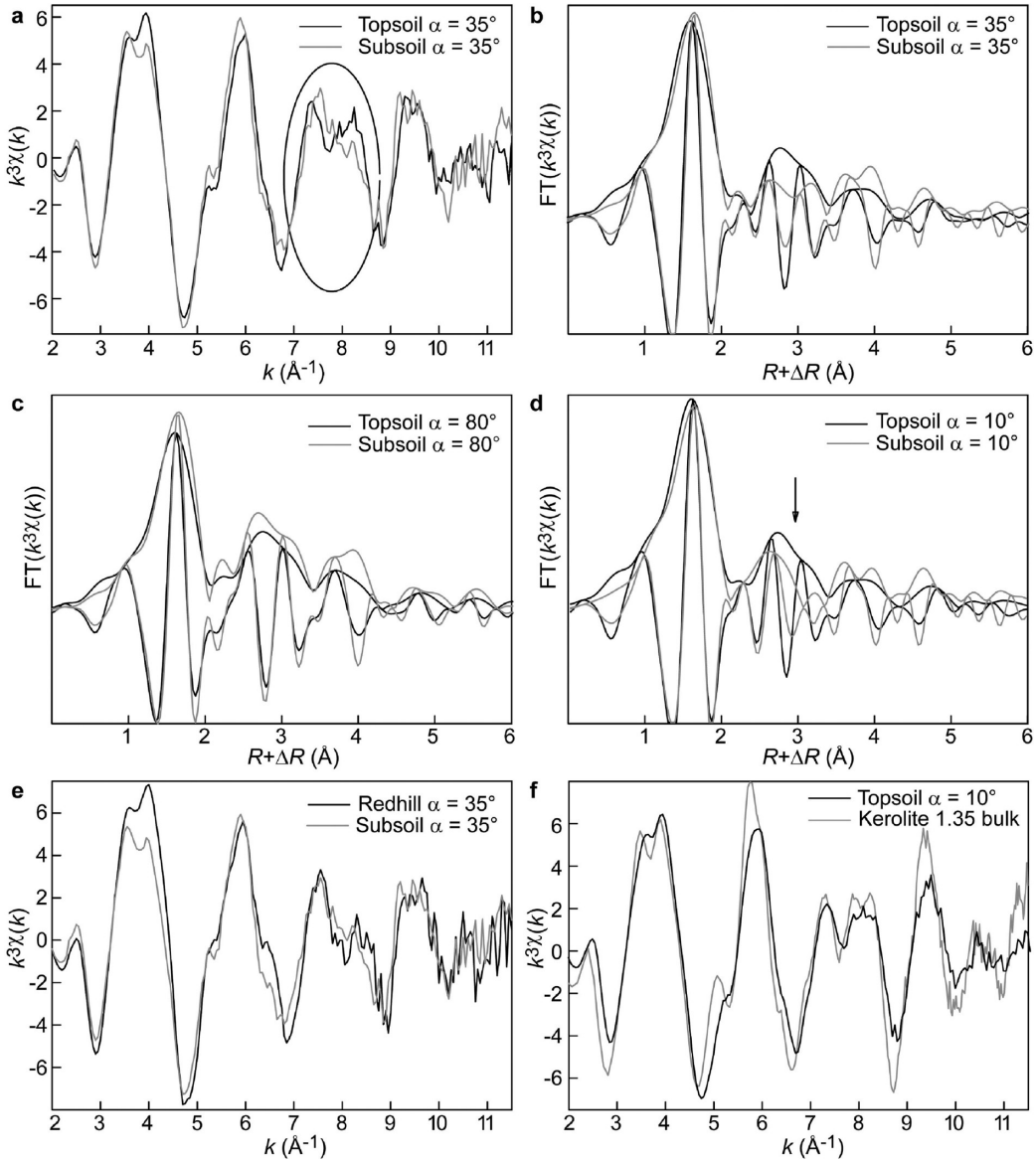

FIGURE 3. Overlay plots of Zn K-edge EXAFS spectra and Fourier transforms of the Aa and Bb clay films at selected measurement angles (a-d) and comparison with Redhill montmorillonite and kerolite spectra (e,f).

Zn, and the neoformed phyllosilicate species present everywhere in the soil matrix represents the main Zn speciation in the entire topsoils.

The fractional amounts of the three other Zn species identified by μ-EXAFS (i.e., Zn bound to Fe and Mn (oxyhydr)oxides and organic matter) were evaluated by linear combination fitting of the pure species spectra to the bulk spectra. Results of this analysis (Figure S3) confirmed quantitatively the overall significance of the Zn phyllosilicate species and minor importance of the other species in the entire topsoils. The reconstructions of the Aa and Ba spectra with neoformed phyllosilicate as a single-component fit were degraded when the organic and phyllomanganate species were included in the fit, indicating that their fractions are less than 10−15% (*4, 6*). Inclusion of 10−15% Zn-sorbed goethite also did not improve the fit, or did so marginally, but did not degrade it either. Therefore, Zn bound to ferric oxyhydroxides likely is the second most abundant species after phyllosilicate. Attempts to include a second component were more successful with the Ca topsoil and suggested the presence of ~25% organic Zn (Figure S3). The detection of organic Zn in this cultivated topsoil and the lower level of Fe oxyhydroxide-bound Zn are consistent with the lesser amounts of anthropogenic Zn and Fe (speciated initially as FeS_2) farther from the smelter.

Zn Phyllosilicates. The P-EXAFS spectra from the neoformed and geogenic Zn phyllosilicates have a marked angular dependence (Figure 2d,e), indicating that the Zn coordination shells are oriented relative to the clay platelets (*27, 34*). An overlay plot of the $k^3\chi_{\alpha=35°}(k)$ spectra from the topsoil and subsoil shows a distinctive pattern at $k = 7.5-8.5$ Å^{-1}, with one oscillation being a doublet (topsoil) and the other tipping at $k = 7.5$ Å^{-1} and being asymmetric to the right (subsoil) (Figure 3a). In real space, this difference manifests itself in the $R+\Delta R = 2.0-3.5$ Å interval (Zn-metal shells), while the first FT peaks at shorter distance (Zn−O shell) show considerable similarity (Figure 3b). Qualitatively, one may conclude that Zn has the same coordination (i.e., tetrahedral or octahedral) at the two depths in the soils, but different nearest (i.e., Al, Fe) and/or next-nearest (i.e., Si) cationic shells (Figure 2c). This ambiguity can be clarified by comparing the out-of-plane ($k^3\chi_{\alpha=80°}$) and in-plane ($k^3\chi_{\alpha=10°}$) structures.

The two FTs have obvious likenesses over the entire $R+\Delta R$ interval at $\alpha = 80°$ but again are distinctly different between 2.0 and 3.5 Å at $\alpha = 10°$ (Figure 3c,d). Comparing the

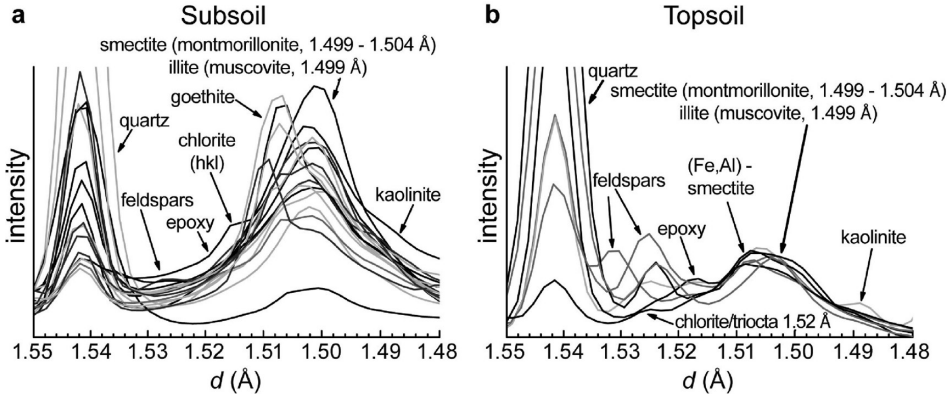

FIGURE 4. μ-XRD traces of the 060 reflections from the clay matrix for the subsoil (a) and topsoil (b). The intensities are normalized to I_0 and exposure time. The 211 quartz reflection at 1.5415 Å was used as internal standard.

imaginary parts of the Fourier transforms at $\alpha = 10°$, we observe a rightward shift of the oscillation at $R+\Delta R \sim 3.0$ Å in the subsoil. Data analysis showed that Zn is surrounded by one O shell at 2.05 Å and two Si shells at 3.22 Å (Si_1) and 4.44 Å (Si_2) in the perpendicular direction of the two clays (Figure S4a, Table S3). This local structure is characteristic of octahedral Zn in a 2:1 phyllosilicate environment (Figure 2c) (*30*). In the parallel orientation the second FT peak at 2.0−3.5 Å for phyllosilicates results primarily from the nearest cationic shell of the octahedral sheet (Me) and, secondarily, from the nearest Si shell (Si_1, Figure 2c). Since the phyllosilicates in the topsoil and subsoil have the same out-of-plane structure, their Si_1 contributions in the in-plane orientation are also the same; thus, the difference in their FTs at $\alpha = 10°$ arises from the Me shell. Data analysis showed that Zn is surrounded by 3 Al at 2.98 Å in the subsoil, as in dioctahedral smectite (Figure S4b). This interpretation is supported also by the similarity of the spectra for the subsoil and Redhill montmorillonite (Figure 3e, SI). In particular, their third EXAFS oscillations exhibit similar shapes.

Since Zn is surrounded by Al atoms in the octahedral sheet of the subsoil phyllosilicate, and the two soil phyllosilicates differ in composition of their Me shells, the octahedral sheet of the topsoil phyllosilicate either contains another type of atom (e.g., Zn or Fe) or a mixture of Al and Zn/Fe atoms. Data analysis and spectral comparison with references showed that the wave doublet at 7 $Å^{-1} < k < 9$ $Å^{-1}$ is produced when Zn atoms are surrounded by 'light' (e.g., Al or Mg) and 'heavy' (e.g., Fe or Zn) atoms (Figures S5 and S6). This is illustrated in Figures 3f and S7 with the trioctahedral smectite kerolite, which forms a continuous solid solution between the Mg ($Si_4Mg_{3.0}O_{10}(OH)_2 \cdot nH_2O$) and Zn ($Si_4Zn_{3.0}O_{10}(OH)_2 \cdot nH_2O$) poles (*14, 30*). Within this reference series, $Si_4Zn_{1.35}Mg_{1.65}O_{10}(OH)_2 \cdot nH_2O$ provided the best match to the $k^3\chi_{\alpha=10°}$ topsoil spectrum, meaning that the Me shell has a ratio of 'heavy' to 'light' atoms close to 1.35/1.65 = 0.8. This ratio is incompatible with a LDH-like local structure, because LDH has a Zn/Al ratio ≥2.0 (*35*). The LDH spectrum is also distinct from the topsoil spectrum (Figure S6a).

This ratio of 0.8 does not give any indication on the total number of Me nearest atoms in the octahedral sheet. Zinc may as well be in a dioctahedral phyllosilicate, in which case it is surrounded by three nearest cations, instead of six as in kerolite. Structural parameters were corefined by analyzing simultaneously the data collected at all angles to increase precision. The data can be simulated equally well with either 2.9 ± 0.5 Al and 3.0 ± 0.5 Fe (trioctahedral hypothesis) or 1.4 ± 0.4 Al and 1.6 ± 0.4 Fe (dioctahedral hypothesis, Figure S4c and Tables S2 and S3).

In summary, P-EXAFS shows that Zn is incorporated in a phyllosilicate framework in both the topsoil and subsoil.

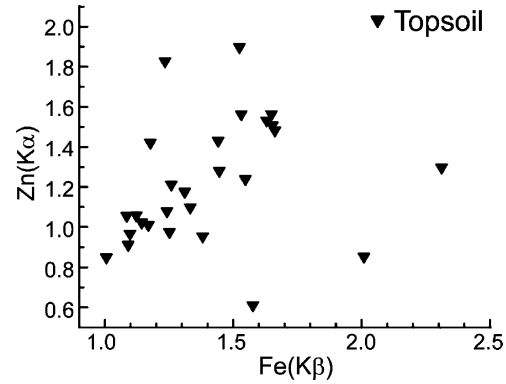

FIGURE 5. Zn and Fe fluorescence counts from the spots analyzed by μ-XRD for the topsoil.

The Zn-containing phyllosilicates do not have the same composition in the two horizons; it is purely aluminous in the subsoil and ferruginous in the topsoil. However, the di- or trioctahedral nature of the phyllosilicate cannot be determined unambiguously by EXAFS, as discussed previously (*36*). This question is addressed below by μ-XRD.

Zn Clay Mineralogy and Composition. The composition of the octahedral sheet can be inferred from the dependence of the *b* unit cell parameter on the site occupancy and size of Me cations (*37*). The clay matrix from the subsoil has a 060 reflection which is symmetric and centered at 1.50 Å, consistent with a dioctahedral phyllosilicate, including montmorillonite, illite, and muscovite (Figure 4a). The three species were identified by measuring the 00l reflections on oriented preparations (SI) (*38*). In some cases a shoulder at 1.49 Å from kaolinite and another at 1.515 Å from chlorite were observed (Figure 4a). Zinc is most likely associated with montmorillonite because kaolinite, Illite, and chlorite platelets cannot be monodispersed in suspension and thus cannot be highly oriented in the plane of the film. The smectite was isolated naturally during the film preparation.

In contrast to the subsoil, the 060 reflection from the clay matrix of the topsoil is most often a doublet with one maximum at 1.501 Å and another at 1.508 Å, and a shape determined by the proportion of the two phyllosilicate populations (Figure 4b). The 1.508 Å reflection is attributed to dioctahedral (Fe,Al)-smectite, because its position is intermediate between those of aluminous (1.501 Å) and ferric smectites (1.52 Å) (*38, 39*), and its intensity varied with the intensity of the Fe(Kβ) signal measured simultaneously to the μ-XRD patterns on the same spots. Zinc always was detected in these spots (Figure 5). A maximum at 1.522 Å, matching a known diffraction peak of trioctahedral chlorite, was detected in some patterns, but there was no peak at 1.53 Å from (Mg,Zn)-kerolite. There was no correlation between

Zn and chlorite. Therefore, the correlation between Fe(Kβ) and the 1.508 Å reflection, the absence of goethite in the clay matrix, and the association of Zn with the (Fe,Al)-smectite, taken together, suggest that Zn is bound to the ferruginous smectite in the topsoil. Also apparent from Figure 5 is that the Zn/Fe ratio varies greatly from one particle to another. The neoformed smectite likely owes its variability in composition to variations in the chemistry of the soil pore solutions. There is no geochemical nor crystallochemical reasons for this ratio to be constant.

Mineralogical Signature of Anthropogenic Zn and Environmental Implications. Dioctahedral ferruginous smectite is the main immobilization form of anthropogenic Zn, since this species is dominant and neoformed in the topsoil. If this phyllosilicate occurred naturally, it would be Fe-free, as observed 30 cm below the surface in the subsoil, where Zn concentration is sixteen (A), six (B), and three (C) times lower and close to the regional geochemical background (68 mg/kg (*25*)). Results presented in the Supporting Information show that the coassociation of Fe and Zn in smectite results from the weathering of Zn and Fe particles (mostly ZnS, ZnO, FeS_2, $ZnFe_2O_4$) from atmospheric deposition and their pervasive diffusion and coprecipitation in the soil clay matrix. This type of Zn sequestration is potentially irreversible, because dioctahedral phyllosilicates are stable over a large pH range (from mildly acidic to basic) and it is how Zn is naturally immobilized in these calcareous soils. Therefore, the incorporation of Zn in the octahedral sheet of montmorillonite is probably a potent mechanism of natural attenuation of the contamination, despite the long-term persistence of this element at the soil surface. Zinc incorporation in trioctahedral phyllosilicates, such as kerolite, and Zn-LDH, not identified in this study, is likely less durable because these phases are thermodynamically less stable than aluminous phyllosilicates.

In this polluted area of approximately 40 km^2 from northern France, the relatively high pH of the ploughed calcareous soils and their liming minimize the potential risk of metal contamination (mostly Pb, Cd, Zn) to wildlife and to crop production. The bioavailability of metals is, however, higher in the surrounding woodlands owing to their neutral to acidic properties and higher metal content in relation with human activities (rubbles, slag and soil deposits) (*40, 41*). In these carbonaceous soils, organic Zn, which is more mobile than Zn-bearing phyllosilicate, may be the dominant species.

Acknowledgments

Jean Louis Hazemann, Sirine Fakra, Matthew Marcus, and Olivier Proux are thanked for their assistance during X-ray measurements. Thanks are extended to Renaud Scheifler and Annette de Vaufleury for setting up the STARTT research program and to Francis Douay for soil analyses and fruitful scientific discussions. This manuscript benefitted from the constructive comments of three anonymous reviewers. This work was supported by the Agence Nationale de la Recherche (ANR) (contract no. ANR-05-ECCO-004). The ALS is supported by the Director, Office of Science, Office of Basic Energy Sciences, Materials Sciences Division of the U.S. Department of Energy under Contract DE-AC03-76SF00098 at the Lawrence Berkeley National Laboratory.

Supporting Information Available

Text, figures, and tables describing sample preparation, methodological details, and additional P-EXAFS and diffraction results. This material is available free of charge via the Internet at http://pubs.acs.org.

Literature Cited

(1) Bi, X.; Feng, X.; Yang, Y.; Qiu, G.; Li, G.; Li, F.; Liu, T.; Fu, Z.; Jin, Z. Environmental contamination of heavy metals from zinc smelting areas in Hezhang County, western Guizhou. *China Environ. Inter.* **2006**, *32*, 883–890.

(2) Mench, M.; Schwitzguebel, J. P.; Schroeder, P.; Bert, V.; Gawronski, S.; Gupta, S. Assessment of successful experiments and limitations of phytotechnologies: contaminant uptake, detoxification and sequestration, and consequences for food safety. *Environ. Sci. Pollut. Res.* **2009**, *16*, 876–900.

(3) Smolders, E.; Oorts, K.; van Sprang, P.; Schoeters, I.; Janssen, C. R.; McGrath, S. P.; McLaughlin, M. J.; Mike, J. Toxicity of trace metals in soil as affected by soil type and aging after contamination using calibrated bioavailability models to set ecological soil standards. *Environ. Toxicol. Chem.* **2009**, *28*, 1633–1642.

(4) Manceau, A.; Marcus, M. A.; Tamura, N., Quantitative speciation of heavy metals in soils and sediments by synchrotron X-ray techniques. In *Applications of Synchrotron Radiation in Low-Temperature Geochemistry and Environmental Science*; Fenter, P. A., Rivers, M. L., Sturchio, N. C., Sutton, S. R., Eds.; Mineralogical Society of America: Washington, DC, 2002; Vol. 49, pp 341−428.

(5) Hansel, C. M.; Fendorf, S.; Sutton, S.; Newville, M. Characterization of Fe plaque and associated metals on the roots of mine-waste impacted aquatic plants. *Environ. Sci. Technol.* **2001**, *35*, 3863–3868.

(6) Isaure, M. P.; Laboudigue, A.; Manceau, A.; Sarret, G.; Tiffreau, C.; Trocellier, P.; Hazemann, J. L.; Chateigner, D. Quantitative Zn speciation in a contaminated dredged sediment by μPIXE, μSXRF, EXAFS spectroscopy and principal component analysis. *Geochim. Cosmochim. Acta* **2002**, *66*, 1549–1567.

(7) Isaure, M. P.; Manceau, A.; Geoffroy, N.; Laboudigue, A.; Tamura, N.; Marcus, M. A. Zinc mobility and speciation in soil covered by contaminated dredged sediment using micrometer-scale and bulk-averaging X-ray fluorescence, absorption and diffraction techniques. *Geochim. Cosmochim. Acta* **2005**, *69*, 1173–1198.

(8) Jacquat, O.; Voegelin, A.; Villard, A.; Marcus, M. A.; Kretzschmar, R. Formation of Zn-rich phyllosilicate, Zn-layered double hydroxide and hydrozincite in contaminated calcareous soils. *Geochim. Cosmochim. Acta* **2008**, *72*, 5037–5054.

(9) Jacquat, O.; Voegelin, A.; Juillot, F. R. K. Changes in Zn speciation during soil formation from Zn-rich limestones. *Geochim. Cosmochim. Acta* **2009**, *73*, 5554–5571.

(10) Van Damme, A.; Degryse, F.; Smolders, E.; Sarret, G.; Dewit, J.; Swennen, R.; Manceau, A. Zinc speciation in mining and smelter contaminated overbank sediments by EXAFS spectroscopy. *Geochim. Cosmochim. Acta* 2010. in press.

(11) Juillot, F.; Morin, G.; Ildefonse, P.; Trainor, T. P.; Benedetti, M.; Galoisy, L.; Calas, G.; Brown, G. E. Occurrence of Zn/Al hydrotalcite in smelter-impacted soils from northern France: Evidence from EXAFS spectroscopy and chemical extractions. *Am. Mineral.* **2003**, *88*, 509–526.

(12) Kirpichtchikova, T.; Manceau, A.; Spadini, L.; Panfili, F.; Marcus, M. A.; Jacquet, T. Speciation and solubility of heavy metals in contaminated soil using X-ray microfluorescence, EXAFS spectroscopy, chemical extraction, and thermodynamic modelling. *Geochim. Cosmochim. Acta* **2006**, *70*, 2163–2190.

(13) Nachtegaal, M.; Marcus, M. A.; Sonke, J. E.; Vangronsveld, J.; Livi, K.; van der Lelie, D.; Sparks, D. L. Effects of in situ remediation on the speciation and bioavailability of zinc in a smelter contaminated soil. *Geochim. Cosmochim. Acta* **2005**, *69*, 4649–4664.

(14) Manceau, A.; Lanson, B.; Schlegel, M. L.; Hargé, J. C.; Musso, M.; Eybert-Bérard, L.; Hazemann, J. L.; Chateigner, D.; Lamble, G. M. Quantitative Zn speciation in smelter-contaminated soils by EXAFS spectroscopy. *Am. J. Sci.* **2000**, *300*, 289–343.

(15) Manceau, A.; Tamura, N.; Celestre, R. S.; MacDowell, A. A.; Geoffroy, N.; Sposito, G.; Padmore, H. A. Molecular-scale speciation of Zn and Ni in soil ferromanganese nodules from loess soils of the Mississippi basin. *Environ. Sci. Technol.* **2003**, *37*, 75–80.

(16) Manceau, A.; Marcus, M. A.; Tamura, N.; Proux, O.; Geoffroy, N.; Lanson, B. Natural speciation of Zn at the micrometer scale in a clayey soil using X-ray fluorescence, absorption, and diffraction. *Geochim. Cosmochim. Acta* **2004**, *68*, 2467–2483.

(17) Manceau, A.; Tommaseo, C.; Rihs, S.; Geoffroy, N.; Chateigner, D.; Schlegel, M.; Tisserand, D.; Marcus, M. A.; Tamura, N.; Chen, Z. S. Natural speciation of Mn, Ni and Zn at the micrometer scale in a clayey paddy soil using X-ray fluorescence, absorption, and diffraction. *Geochim. Cosmochim. Acta* **2005**, *69*, 4007–4034.

(18) Manceau, A.; Lanson, M.; Geoffroy, N. Natural speciation of Ni, Zn, Ba and As in ferromanganese coatings on quartz using X-ray fluorescence, absorption, and diffraction. *Geochim. Cosmochim. Acta* **2007**, *71*, 95–128.
(19) Ndiba, P.; Axe, L.; Boonfueng, T. Heavy metal immobilization through phosphate and thermal treatment of dredged sediments. *Environ. Sci. Technol.* **2008**, *42*, 920–926.
(20) Panfili, F.; Manceau, A.; Sarret, G.; Spadini, L.; Kirpichtchikova, T.; Bert, V.; Laboudigue, A.; Marcus, M. A.; Ahamdach, N.; Libert, M. F. The effect of phytostabilization on Zn speciation in a dredged contaminated sediment using scanning electron microscopy, X-ray fluorescence, EXAFS spectroscopy and principal components analysis. *Geochim. Cosmochim. Acta* **2005**, *69*, 2265–2284.
(21) Roberts, D. R.; Scheinost, A. C.; Sparks, D. L. Zinc speciation in a smelter-contaminated soil profile using bulk and microscopic techniques. *Environ. Sci. Technol.* **2002**, *36*, 1742–1750.
(22) Sarret, G.; Balesdent, J.; Bouziri, L.; Garnier, J. M.; Marcus, M. A.; Geoffroy, N.; Panfili, F.; Manceau, A. Zn speciation in the organic horizon of a contaminated soil by micro X-ray fluorescence, micro and powder EXAFS spectroscopy and isotopic dilution. *Environ. Sci. Technol.* **2004**, *38*, 2792–2801.
(23) Scheinost, A. C.; Kretzschmar, R.; Pfister, S.; Roberts, D. R. Combining selective sequential extractions, X-ray absorption spectroscopy and principal component analysis for quantitative zinc speciation in soil. *Environ. Sci. Technol.* **2002**, *36*, 5021–5028.
(24) Schuwirth, N.; Voegelin, A.; Kretzschmar, R.; Hofmann, T. Vertical distribution and speciation of trace metals in weathering flotation residues of a zinc/lead sulfide mine. *J. Environ. Qual.* **2007**, *36*, 61–69.
(25) Douay, F.; Pruvot, C.; Waterlot, C.; Fritsch, C.; Fourrier, H.; Loriette, A.; Bidar, G.; Grand, C.; de Vaufleury, A.; Scheifler, R. Contamination of woody habitat soils around a former lead smelter in the North of France. *Sci. Total Environ.* **2009**, *407*, 5564–5577.
(26) Proux, O.; Nassif, V.; Prat, A.; Ulrich, O.; Lahera, E.; Biquard, X.; Menthonnex, J. J.; Hazemann, J. L. Feedback system of a liquid-nitrogen-cooled double-crystal monochromator: design and performances. *J. Synchrotron Radiat.* **2006**, *13*, 59–68.
(27) Manceau, A.; Chateigner, D.; Gates, W. P. Polarized EXAFS, distance-valence least-squares modeling (DVLS) and quantitative texture analysis approaches to the structural refinement of Garfield nontronite. *Phys. Chem. Miner.* **1998**, *25*, 347–365.
(28) Manceau, A.; Bonnin, D.; Stone, W. E. E.; Sanz, J. Distribution of Fe in the octahedral sheet of trioctahedral micas by polarized EXAFS. Comparison with NMR results. *Phys. Chem. Miner.* **1990**, *17*, 363–370.
(29) Marcus, M. A.; MacDowell, A. A.; Celestre, R.; Manceau, A.; Miller, T.; Padmore, H. A.; Sublett, R. E. Beamline 10.3.2 at ALS: a hard X-ray microprobe for environmental and materials sciences. *J. Synchrotron Radiat.* **2004**, *11*, 239–247.
(30) Schlegel, M. L.; Manceau, A.; Charlet, L.; Hazemann, J. L. Adsorption mechanism of Zn on hectorite as a function of time, pH, and ionic strength. *Am. J. Sci.* **2001**, *301*, 798–830.
(31) Depège, C.; El Metoui, F. Z.; Forano, C.; De Roy, A.; Dupuis, J.; Besse, J. P. Polymerization of silicates in layered double hydroxides. *Chem. Mater.* **1996**, *8*, 952–960.
(32) Ford, R. G.; Sparks, D. L. The nature of Zn precipitates formed in the presence of pyrophyllite. *Environ. Sci. Technol.* **2000**, *34*, 2479–2483.
(33) Voegelin, A.; Pfister, S.; Scheinost, A. C.; Marcus, M. A.; Kretzschmar, R. Changes in zinc speciation in field soil after contamination with zinc oxide. *Environ. Sci. Technol.* **2005**, *39*, 6616–6623.
(34) Furnare, L. J.; Vailionis, A.; Strawn, D. G. Polarized XANES and EXAFS spectroscopic investigation into copper(II) complexes on vermiculite. *Geochim. Cosmochim. Acta* **2005**, *69*, 5219–5231.
(35) Bellotto, M.; Rebours, B.; Clause, O.; Lynch, J.; Bazin, D.; Elkaim, E. A reexamination of hydrotalcite crystal chemistry. *J. Phys. Chem.* **1996**, *100*, 8527–8534.
(36) Manceau, A. Distribution of cations among the octahedra of phyllosilicates: insight from EXAFS. *Can. Mineral.* **1990**, *28*, 321–328.
(37) Drits, V. A.; Dainyak, L. G.; Muller, F.; Besson, G.; Manceau, A. Isomorphous cation distribution in celadonites, glauconites and Fe-illites determined by infrared, Mossbauer and EXAFS spectroscopies. *Clay Miner.* **1997**, *32*, 153–179.
(38) Brindley, G. W.; Brown, G. *Crystal structures of clay minerals and their X-ray identification*; Mineralogical Society: London, 1980; p 495.
(39) Srodon, J.; Drits, V. A.; McCarty, D. K.; Hsieh, J. C. C.; Eberl, D. D. Quantitative X-ray diffraction analysis of clay-bearing rocks from random preparations. *Clays Clay Miner.* **2001**, *49*, 514–528.
(40) Fritsch, C.; Cosson, R. P.; Coeurdassier, M.; Raoul, F.; Giraudoux, P.; Crini, N.; de Vaufleury, A.; Scheifler, R. Responses of wild small mammals to a pollution gradient: Host factors influence metal and metallothionein levels. *Environ. Pollut.* **2010**, *158*, 827–840.
(41) Fritsch, C.; Giraudoux, P.; Coeurdassier, M.; Douay, F.; Raoul, F.; Pruvot, C.; Waterlot, C.; de Vaufleury, A.; Scheifler, R. Spatial distribution of metals in smelter-impacted soils of woody habitats: Influence of landscape and soil properties, and risk for wildlife. *Chemosphere*, doi:10.1016/j.chemosphere.2010.06.075.

ES101567U

SUPPORTING INFORMATION FOR

Natural Attenuation of Zinc Pollution in Smelter-Affected Soil

M. Vespa[†], M. Lanson, A. Manceau*

Mineralogy & Environments Group, ISTerre, University Joseph Fourier and CNRS, 38041 Grenoble Cedex 9, France

† Present address: Institute for Transuranium Elements, Joint Research Centre, Postfach 2340, D-76125 Karlsruhe, Germany

Number of pages: 18

Number of Tables: 3

Number of Figures: 11

1. Materials and Methods

1.1. Soil samples

Samples from the three topsoils (<15 cm) and subsoils (35-50 cm) were dried and sieved to <2 mm. The zinc concentration and main physiochemical properties are reported in Table S1.

Table S1. Zn total content and physiochemical properties of the three soil samples (A, B, C) at the two sampling depths (a, b);

		Aa	Ba	Ca	Ab	Bb	Cb
		Topsoil	**Topsoil**	**Topsoil**	**Subsoil**	**Subsoil**	**Subsoil**
Depths	**cm**	0-15	0-15	0-15	35-50	35-50	35-50
pH[1]		7.9	7.0	7.9	8.4	7.7	8.1
TOC[2]	**g/kg**	60.5	30.2	37.0	9.9	9.2	12.9
$CaCO_3$ total[3]	**g/kg**	120.0	<1	2.7	160.0	<1	1.2
Clays[4]	**g/kg**	240	278	330	199	248	446
Silt[4]	**g/kg**	634	584	414	660	574	419
Sand[4]	**g/kg**	126	138	256	141	178	135
Zn total in soils[5]	**mg/kg**	1092	430	287	69	67	102
exchangeable Zn in soils	**mg/kg**	10	14	0.4	0	0	0
Zn total in <2 µm clay fraction[6]	**mg/kg**	2550	1090	610	140	160	160
exchangeable Zn in <2 µm fraction	**mg/kg**	0	0	0	0	0	0

Analytical methods: 1 = NF ISO 10390; 2 = NF ISO 10694; 3 = NF ISO 10693; 4 = NF X31-107; 5 = Calcination at 450°C and a mixture of hydrofluoric (HF) and perchloric ($HClO_4$) acids, as described by the NF X 31-147 (1996) standard, were used for the total dissolution of Zn. Dissolved Zn was analyzed by ICP-AES; 6 = ICP-AES following the procedure of Laird et al. (*1*). All analyses were performed by INRA in Arras, France, except N° 6 performed at ISTerre.

1.2. Extraction of the <2 µm clay fraction

The <2 µm clay fraction was separated from the < 2 mm bulk fraction by agitation overnight on an orbital shaker followed by centrifugation. This gentle size fractionation is unlikely to have destroyed all soil aggregates enriched in Fe and Mn oxides, in contrast to the more common dispersion method by sonication.

1.3. Measurement of exchangeable Zn

The <2 mm fractions were reacted with 1 M $CaCl_2$, and the <2 µm fractions with 0.5 M NaCl. All samples were shaken for 30 minutes, and Zn in the supernatant was analyzed by ICP-AES.

1.4. Sample preparation for polarized-EXAFS

Highly oriented self-supporting films were prepared from the <2 µm fraction treated first with 30% H_2O_2 to oxidize organic matter (pH 4.2), then with citrate-dithionite–bicarbonate (DCB, pH 5.2) to

dissolve poorly crystallized Fe and Mn oxyhydroxides, according to the procedure described by Mehra and Jackson (*2*). Interlayer cations were exchanged with sodium to improve the dispersion of the clay platelets and the suspensions were filtered on a 0.4 μm Millipore polycarbonate filter at constant flow of one drop per minute. Excess salt on the films was rinsed with deionized water before drying at room temperature. The dried films were cut into slices and stacked on a sample holder to obtain an optimal thickness for fluorescence-yield EXAFS measurement.

The same acetic acid concentration of 0.3 M as in the protocole of Mehra and Jackson (*2*) was used to preserve as much as possible other possible Zn phases, such as Zn-LDH, which otherwise is dissolved readily at 1 M and pH 6 (*3*). Still, this elusive and easily soluble phase perhaps was not totally immune to the chemical treatment, therefore it is not possible to come to unequivocal conclusion concerning its occurrence on the sole basis of P-EXAFS results. More definite conclusion was obtained by μ-EXAFS because this technique is more species sensitive than powder and polarized EXAFS, which both are bulk techniques. If this species were abundant, it would have been detected most likely by μ-EXAFS, as shown in other studies (*3-6*).

1.5. Micro X-ray fluorescence and diffraction

Micro XRF and XRD data were collected on beamline 10.3.2 in transmission mode. The distributions of Zn, Fe, and Mn were imaged from the Zn(Kα), Fe(Kβ), and Mn(Kα) intensities by scanning the sample at an incident energy of 12985 eV (Pb L_3 – 50 eV). The distribution of Pb was imaged by subtracting the normalized As(Kα) intensity measured at 12985 eV from the As(Kα) + Pb(Lα) intensity at 13085 eV (Pb L_3 + 50 eV). Diffraction patterns were measured with a 16 (H) x 7 (V) μm beam size at an energy of 17000 eV using a Bruker CCD camera. The two-dimensional patterns were calibrated with crystalline Al_2O_3 and radially integrated with FIT2D. In addition, the (211) quartz reflection at 1.5415 ± 0.0005 Å was used as internal calibrant to refine the exact position of the 060 reflection of phyllosilicates. Micro X-ray fluorescence spectra were measured simultaneously to μ-XRD with a multichannel analyser (MCA) connected to a seven-element Ge detector. The MCA data were deadtime corrected and normalized to Compton scattering.

1.6. EXAFS data reduction

All EXAFS spectra were extracted from raw data with the Athena interface of the IFFEFIT software (*7, 8*). The Fourier transforms (FT) were obtained from the $k^3\chi(k)$ functions using a Kaiser-Bessel window function with an apodization parameter of 1. The FT peaks of interest were

selected and fitted in reciprocal space with the Artemis interface of the IFFEFIT software. Amplitude and phase shifts functions were calculated using FEFF 8.20 (*9*), and the amplitude reduction factor S_0^2 was set to 0.85 (*10, 11*).

In polarized-EXAFS (P-EXAFS) one detects an apparent coordination number ($CN_{j,\alpha}^{exafs}$), which is the effective number of atoms seen at the angle α (*12*):

$$CN_{j,\alpha}^{exafs} / CN_j = 1 - \left(\left(3\cos^2\beta_j - 1\right)\cdot\left(3\cos^2\alpha - 2\right)\right)/2 \qquad (1)$$

with α = the angle between the electric field vector (**ε**) and the layer plane, β_j = the angle between the film normal and the vector ($\mathbf{R}_{ij}$) connecting the X-ray absorbing atom *i* to the backscattering atom *j*, CN_j = the crystallographic number of atoms in the *j* shell. The P-EXAFS dependency is independent from β_j for $\alpha = 35°$ ($CN_j = CN_{j,\alpha}^{exafs}$) (*11, 13*).

Throughout the data analysis, which was performed on the inverse Fourier transforms (FT^{-1}) of the first and second shells, the numbers of degrees of freedom in the least-squares refinement were reduced by co-varying $CN_{j,\alpha}^{exafs}$ and α, through a polarization parameter which was calculated using β_j angles of 57° for the oxygen shell, 32° for the tetrahedral shell, and 90° for the octahedral shell (*14*). The goodness of the least-squares refinement was evaluated using the reduced chi-square and the *R*-factor (http://cars.uchicago.edu/~newville/feffit/feffit.ps).

The reduced chi-square χ_ν^2 is the statistical parameter minimized by feffit in a fit:

$$\chi_\nu^2 = \frac{N_{idp}}{\nu N \varepsilon^2}\sum_{i=1}^{N}\left[k^3\cdot\chi_{data}(k_i) - k^3\cdot\chi_{model}(k_i)\right]^2 \qquad (2)$$

where $\nu = N_{idp} - N_{var}$ is the number of degrees of freedom in the fit; N_{idp} is the number of independent points $N_{idp} = \frac{2(k_{max}-k_{min})(R_{max}-R_{min})}{\pi} + 2$ (*15*), and N_{var} is the number of variables in the fit. ε is the uncertainty of the measurement. When there are no systematic errors and the statistical errors are measured correctly, the normalized quantity is $\chi_\nu^2 = 1$

The goodness of the fits was quantified by the *R* factor, defined as:

$$R = \frac{\sum_{i=1}^{N}\left[k^3\cdot\chi_{data}(k_i) - k^3\cdot\chi_{model}(k_i)\right]^2}{\sum_{i=1}^{N}\left[k^3\cdot\chi_{data}(k_i)\right]^2} \qquad (3)$$

2. Results and Interpretations

2.1. Zn speciation and dominant species

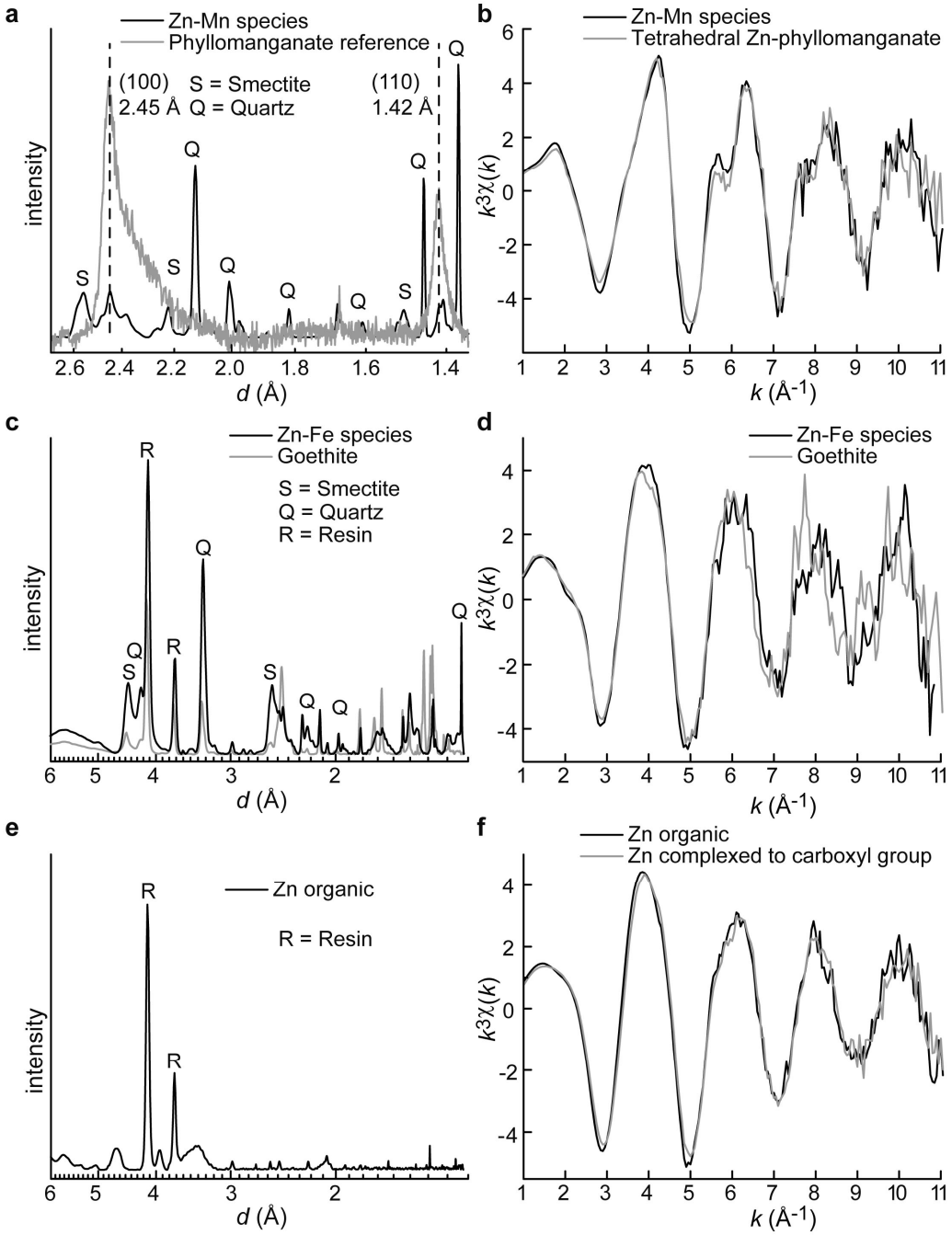

Figure S1. Micro XRD patterns and EXAFS spectra from three of the four Zn associations shown in Figure S2a.

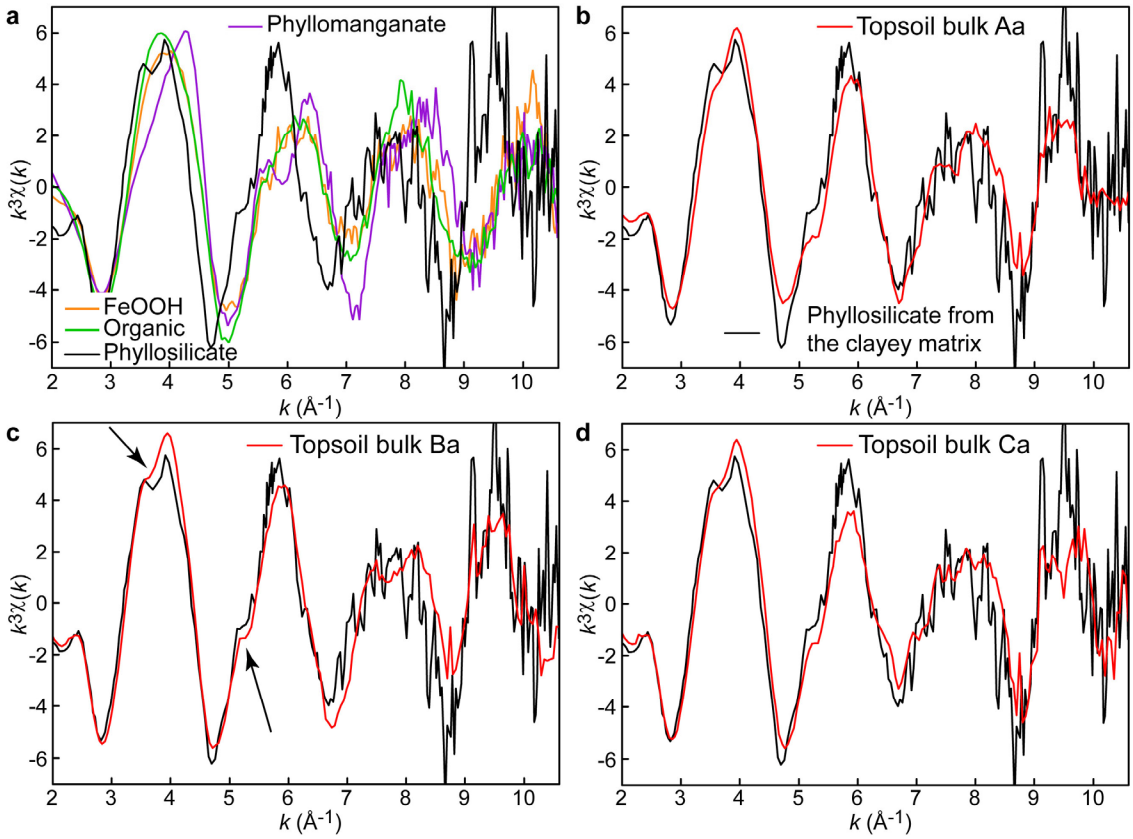

Figure S2. (a) Zn K-edge μ-EXAFS spectra of the four metal species identified in the three topsoils. (b-d) Comparison of the μ-EXAFS spectrum for the Zn phyllosilicate species in (a) with the powder EXAFS spectra from the <2 mm fractions of the three topsoils. The weighted averages of all the Zn species present in the entire topsoils are well described with the μ-EXAFS spectrum collected in the clayey matrix.

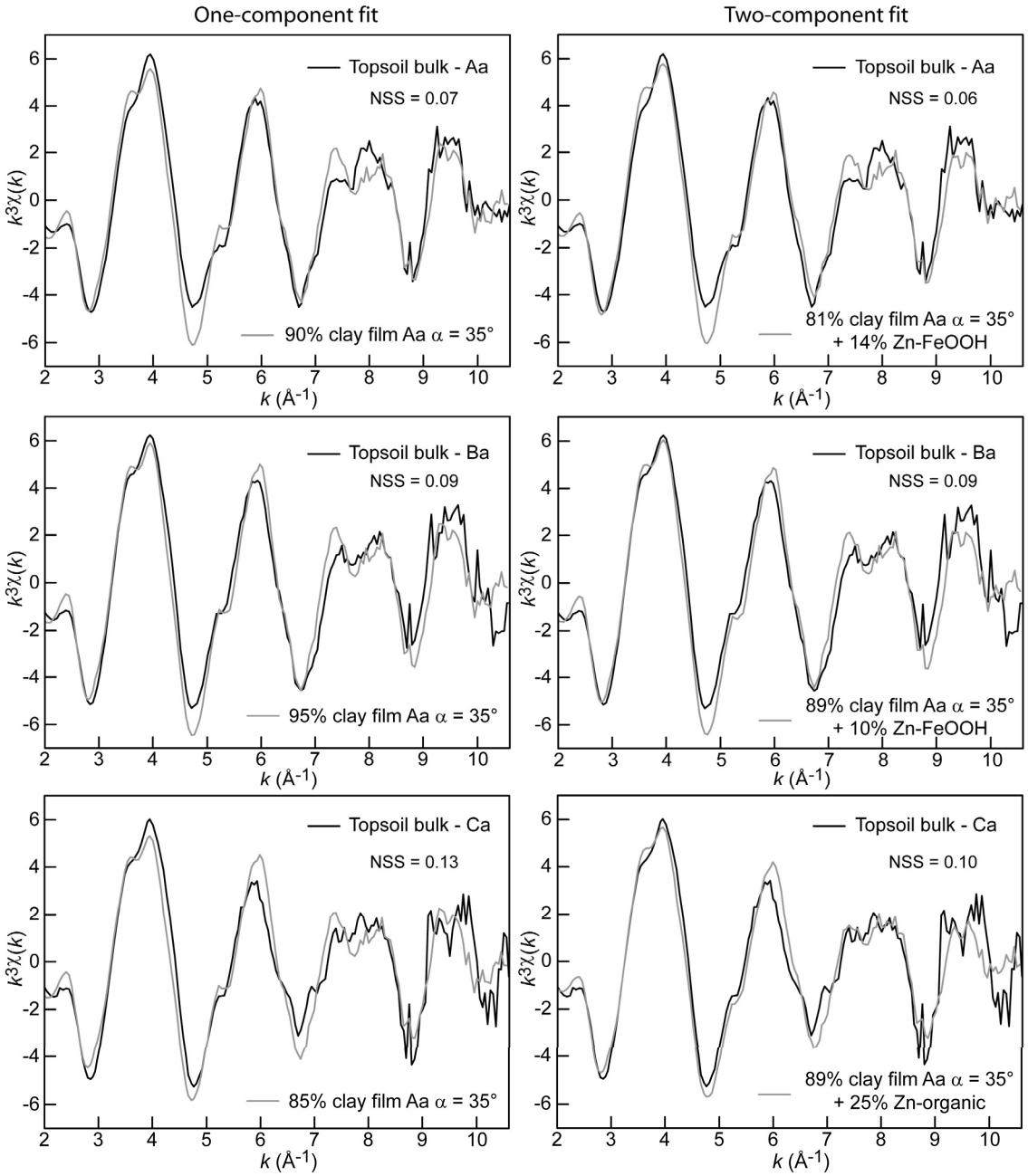

Figure S3. One-component (left column) and two-component (right column) fits of the three topsoil spectra with pure species spectra. The Zn phyllosilicate species is always dominant.

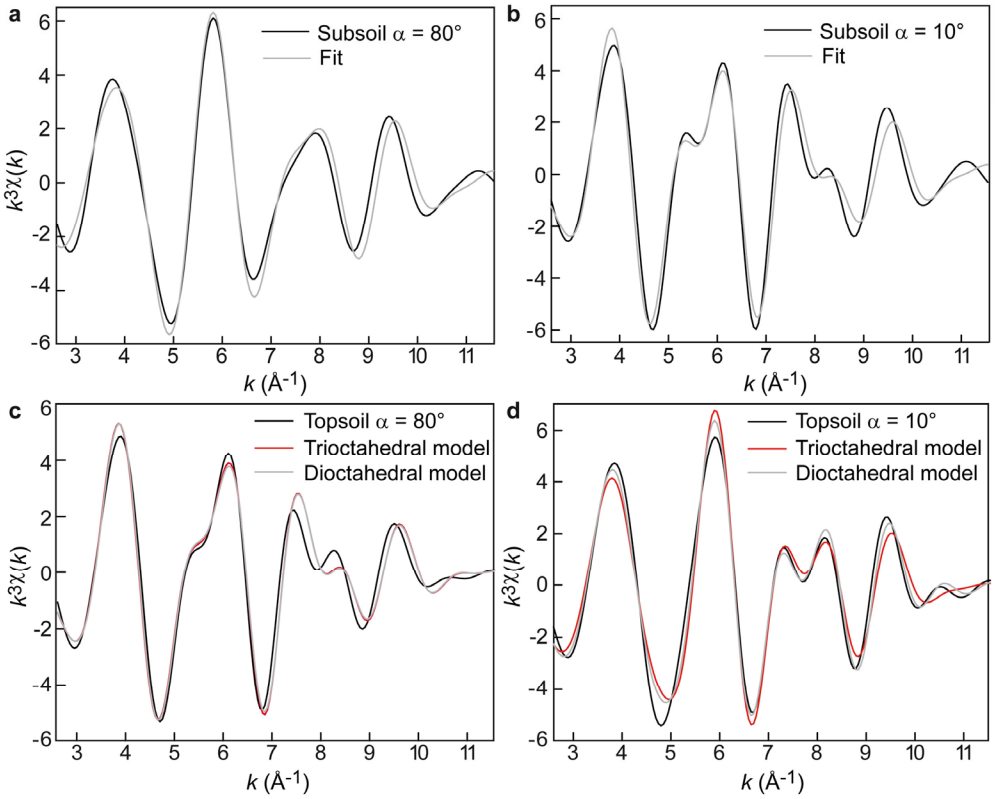

Figure S4. Fourier-filtered EXAFS data in the 1 Å < $R + \Delta R$ < 3.4 Å interval and least-squares fits for the two clay films at α = 10° and 80°. Best-fit parameters are listed in Table S3.

2.2. Bonding environment of Zn

2.2.1. Subsoil

The EXAFS spectrum and FT of the subsoil are dissimilar to those of Zn-Al layered double hydroxide (Zn-Al LDH), indicating that this phase is not observed. It was identified in some soils and may form in contact with hydrous aluminosilicate (*3, 16, 17*) (Figures S5a,b). Sorption of Zn on dioctahedral clays, such as montmorillonite, also can be discarded from the marked differences in frequency, shape and amplitude of the soil and reference spectra (Figure S5c,d). In contrast, a decent match is observed with Zn sorbed on hectorite, a trioctahedral clay (Figure S5e), but the two FTs are distinct in the 2.0 - 3.5 Å $R + \Delta R$ interval (Figure S5f), pointing out differences in the nature and number of Zn-(Me,Si_1) pairs. Finally, the incorporation of Zn in a trioctahedral Mg phyllosilicate, such as kerolite ($Si_4Zn_{1.3}Mg_{1.65}O_{10}(OH)_2$ (*14*)), also is excluded because of the high number of Zn-Mg pairs in the reference which are lacking in the unknown (Figure S5h).

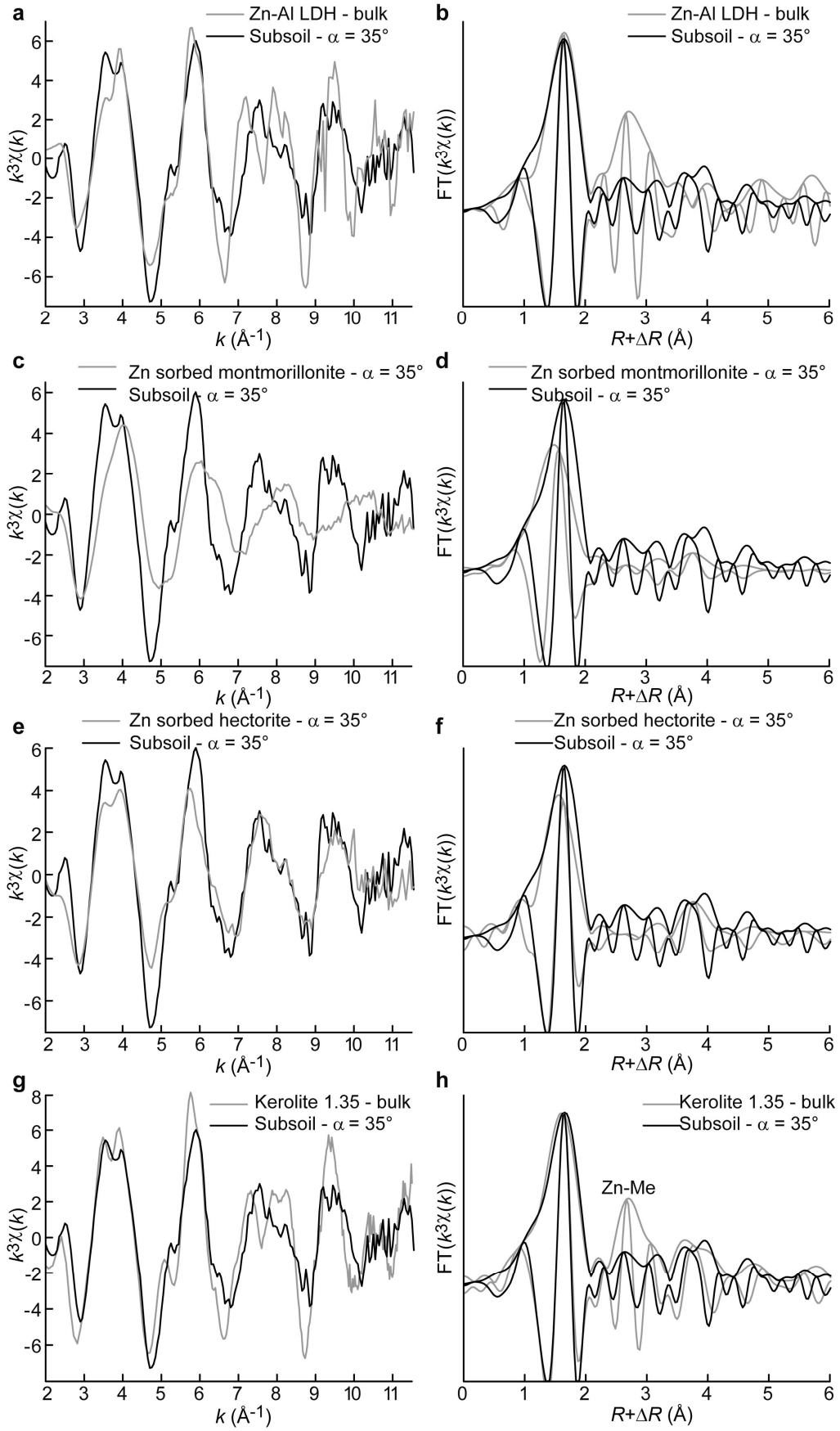
a
Zn-Al LDH - bulk
Subsoil - α = 35°
k3χ(k)
k (Å-1)
b
Zn-Al LDH - bulk
Subsoil - α = 35°
FT(k3χ(k))
R+ΔR (Å)
c
Zn sorbed montmorillonite - α = 35°
Subsoil - α = 35°
k3χ(k)
k (Å-1)
d
Zn sorbed montmorillonite - α = 35°
Subsoil - α = 35°
FT(k3χ(k))
R+ΔR (Å)
e
Zn sorbed hectorite - α = 35°
Subsoil - α = 35°
k3χ(k)
k (Å-1)
f
Zn sorbed hectorite - α = 35°
Subsoil - α = 35°
FT(k3χ(k))
R+ΔR (Å)
g
Kerolite 1.35 - bulk
Subsoil - α = 35°
k3χ(k)
k (Å-1)
h
Kerolite 1.35 - bulk
Subsoil - α = 35°
Zn-Me
FT(k3χ(k))
R+ΔR (Å)

Figure S5. k^3-weighted EXAFS and Fourier transforms (modulus and imaginary parts) of the Zn K-edge spectra for the subsoil at α = 35° compared with references: (a,b) Zn-Al LDH (Zn layered double hydroxide, (*18*)); (c,d) Zn sorbed montmorillonite (dioctahedral clay (*19*)); (e,f) Zn sorbed hectorite (trioctahedral clay (*14*)); and (g,h) Zn-substituted kerolite (trioctahedral clay (*20*)).

2.2.2. Topsoil

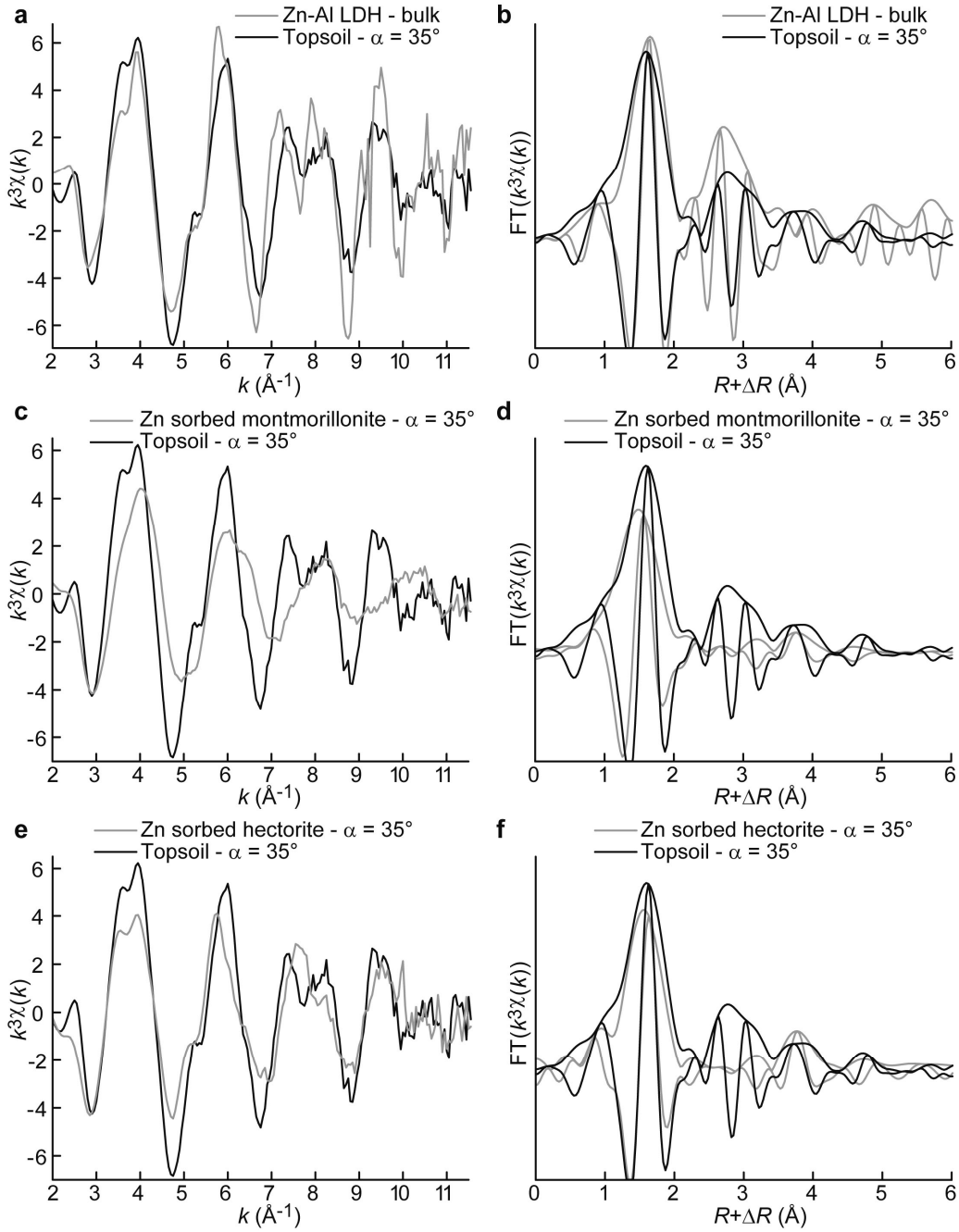

Figure S6. k^3-weighted EXAFS and Fourier transforms of the Zn K-edge spectra for the topsoil at α = 35° compared with references: (a,b) Zn-Al LDH (Zn layered double hydroxide, (*18*)); (c,d) Zn sorbed montmorillonite (*19*); (e,f) Zn-sorbed hectorite (*14*).

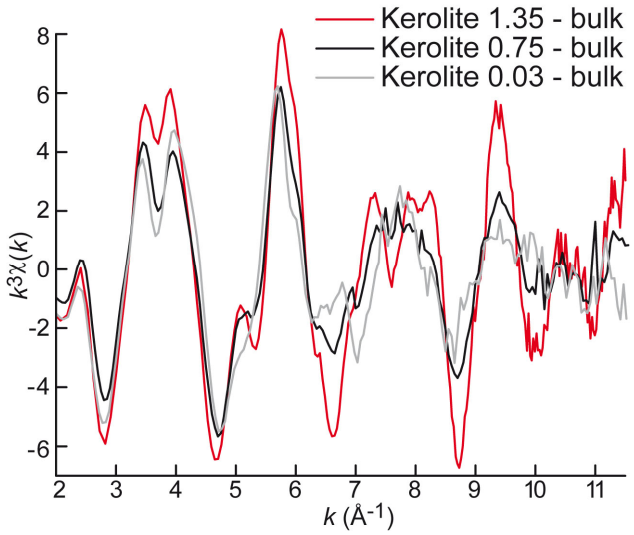

Figure S7. k^3-weighted EXAFS spectra of kerolite at varying Zn/Mg ratios : kerolite 1.35 $Zn_{1.35}Mg_{1.65}.Si_4O_{10}(OH)_2$, kerolite 0.75 ($Zn_{0.75}Mg_{2.25}.Si_4O_{10}(OH)_2$, and kerolite 0.03 $Zn_{0.03}Mg_{2.97}.Si_4O_{10}(OH)_2$ (*14, 21*).

Similarly to the subsoil, spectral comparisons with references show that neither Zn-Al LDH, nor Zn sorbed on montmorillonite and kerolite are likely candidate species for Zn in the topsoil (Figure S6). However, the split structure at k = 7 - 8 Å^{-1} of the topsoil spectra, which is a major distinction to the subsoil samples, is observed also in Zn-substituted kerolites (Figure S7). The dip becomes more prominent when the Zn/Mg ratio increases, and thus is sensitive to the chemical composition of the octahedral sheet.

2.3. P-EXAFS from the clay fraction

2.3.1. Qualitative P-EXAFS data analysis

The P-EXAFS spectra from the topsoil (sample Aa) and the subsoil (sample Bb) have a marked angular dependence, indicating that the local structural environment of Zn is anisotropic and, specifically, that its coordination shells are oriented with respect to clay layers (Figures 3d,e). In addition, Figure S8 shows that the anisotropy of the P-EXAFS signal arises essentially from the contribution of the nearest (Me = Al/Mg and/or Zn/Fe) and next-nearest (Si_1) shells, with the former enhanced in the parallel and the latter in the perpendicular orientation. The weaker angular dependence of the Zn-(Me,Si_1) pairs for the topsoil relative to the subsoil is a strong indication that the Me shell differs in the two clays.

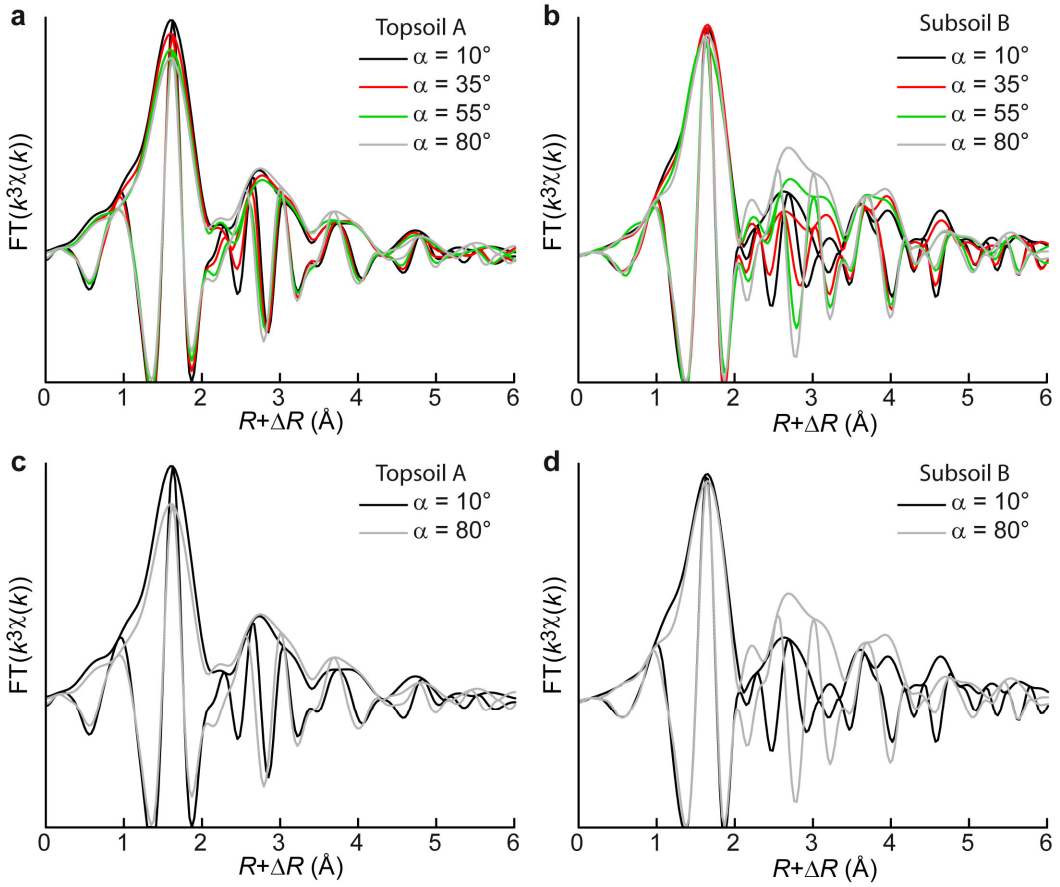

Figure S8. Fourier transforms of the P-EXAFS spectra for the topsoil (sample Aa**)** and subsoil (sample Bb). The anisotropy of the Zn-(Me,Si_1) pairs is more apparent when measurements at intermediate angles are omitted from the plots (c,d).

2.3.2. Quantitative P-EXAFS data analysis

Usually, P-EXAFS data are analyzed by modeling each angle spectrum separately. Here, EXAFS parameters were determined from the corefinement of data recorded at the four α angles to decrease correlations (*22, 23*). Several model fits to the data were attempted, and the significance of each try evaluated from the examination of the correlation matrix. All fit strategies are summarized in Table S2 and results given in Table S3.

2.3.2.1. Redhill reference

To exemplary show and test our fitting approach, the data of Redhill montmorillonite from Manceau et al (Figure S9, *24*) were reanalyzed with the Artemis program (*7, 8*). Zn in Redhill is dioctahedrally coordinated and surrounded by 3 nearest Al atoms in the octahedral sheet and 4 next-nearest Si in the tetrahedral sheet. Therefore, in the first try $CN_{Zn\text{-}O}$, $CN_{Zn\text{-}Al}$ and $CN_{Zn\text{-}Si}$ were fixed at $\alpha = 35°$ to 6, 3 and 4, respectively, and $CN_{j,\alpha}$ fixed using Eq. (1), leaving 7 free running

parameters in the refinement : $R_{Zn\text{-}O}$, $\sigma_{Zn\text{-}O}$, $R_{Zn\text{-}Al}$, $\sigma_{Zn\text{-}Al}$, $R_{Zn\text{-}Si}$, $\sigma_{Zn\text{-}Si}$, ΔE_0 (Tables S2, S3). The refined interatomic distances are $R_{Zn\text{-}O}$ = 2.04 Å, $R_{Zn\text{-}Al}$ = 2.98 Å and $R_{Zn\text{-}Si}$ = 3.21 Å, and all consistent with a phyllosilicate structure. However, despite the seemingly good agreement between experimental data and theoretical model (i.e., low reduced χ^2 and R values), and acceptable values of structural parameters, their precision may be degraded by the correlation of ΔE_0 with $R_{Zn\text{-}Si}$ (0.81), and $R_{Zn\text{-}O}$ (0.78, Table S3).

To evaluate the significance of the previous fit parameters, $CN_{Zn\text{-}Si}$ was subsequently fixed to 3.22 Å, as reported in the literature (*14, 19*) (Figure S10). Results show that ΔE_0 and $R_{Zn\text{-}O}$ were now moderately correlated (0.60), and all other parameters independent. However, decreasing the number of free parameters from 7 to 6 had almost no effect on $R_{Zn\text{-}O}$, $R_{Zn\text{-}Al}$, and $R_{Zn\text{-}Si}$.

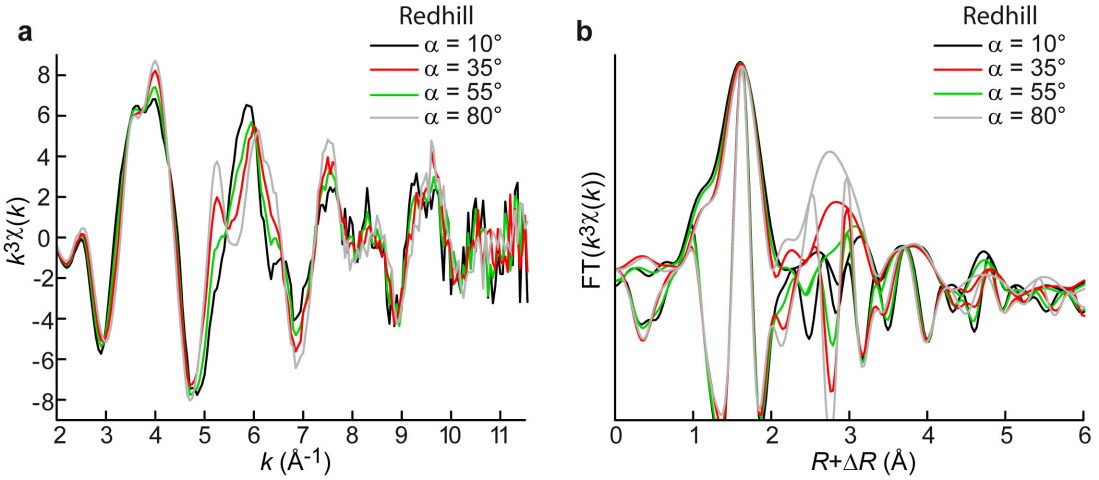

Figure S9. k^3-weighted EXAFS and Fourier transforms of Zn K-edge P-EXAFS spectra for Redhill montmorillonite, a natural Zn-containing dioctahedral smectite (*24*).

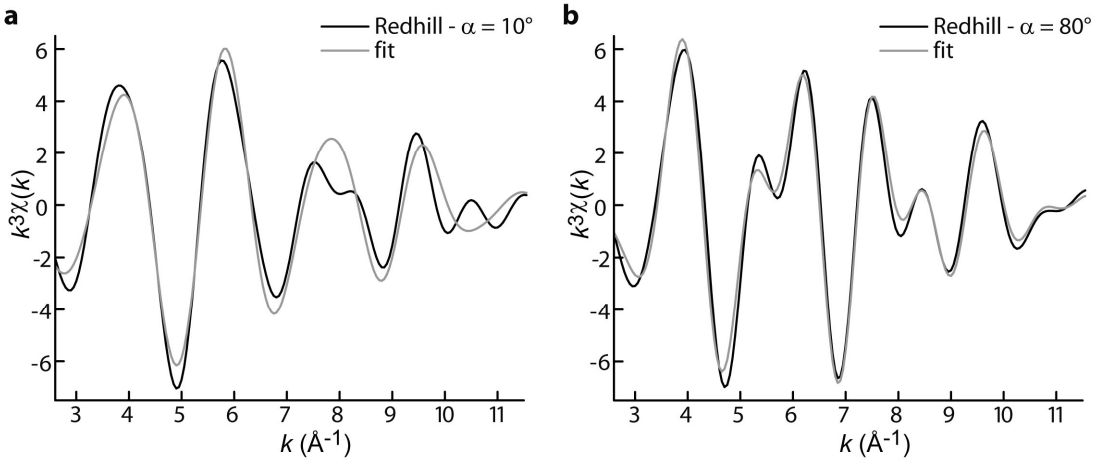

Figure S10. Fourier-filtered EXAFS data in the 1 Å < $R + \Delta R$ < 3.4 Å interval and least-squares fits at α = 10° (a) and α = 80° (b).

2.3.2.2. Subsoil

Similar fit strategies were applied to the subsoil clay. Varying all structural parameters during the simulation (fit 1, Table S3) yields high correlations between *CN* and the Debye-Waller factor σ^2 (0.83 - 0.86 Å^2), making coordination numbers meaningless. When the three *CN* values are fixed to 6, 3 and 4 at $\alpha = 35°$ (fit 2), as for Redhill, not only the *CN*-σ^2 correlation disappears, but in addition σ values are similar to those obtained for Redhill (Table S3). This exact solution was not reached in fit 1 because the minimum being sought was in a deep flat-bottomed valley generated by the high degree of correlations between parameters. Similarly to Redhill, decorrelating ΔE_0 - $R_{Zn\text{-}Si}$ and ΔE_0 - $R_{Zn\text{-}O}$ by fixing $R_{Zn\text{-}Si}$ to 3.22 Å did not modify significantly the other metrical parameters of the best theoretical model to the raw data (fit 3).

2.3.2.3. Topsoil

To test whether Zn is in a trioctahedral environment, $CN_{Zn\text{-}Al} + CN_{Zn\text{-}Fe}$ was set to 6, and the other parameters constrained on the basis of previous results obtained for Redhill and subsoil to limit correlations. In addition, $\sigma_{Zn\text{-}Al}$ and $\sigma_{Zn\text{-}Fe}$ were specified to be identical, as usually the case for Me-Me shells in the EXAFS analysis of phyllosilicates, but $R_{Zn\text{-}Fe}$ was optimized independently from the other interatomic distances. Seven parameters were adjusted for a total of four shells (O, Al, Fe and Si) and 47 independent parameters. The best-fit Zn-O (2.05 Å) and Zn-Fe (3.08 Å) distances are typical of octahedral Zn in ferruginous phyllosilicate. In this fit model, the two Me sub-shells have the same number of atoms ($CN_{Zn\text{-}Al} \approx CN_{Zn\text{-}Fe} = 3.0 \pm 0.5$), and their factor is higher than usual (0.015 Å^2). This result suggests that $CN_{Zn\text{-}Al} + CN_{Zn\text{-}Fe} < 6$, because an excess of coordination is compensated generally by an increase of disorder due to the positive correlation between *CN* and σ^2 in EXAFS (*22, 23*). Consequently, it should be possible to obtain a more meaningful simulation by assuming that Zn is in a dioctahedral clay structure.

In the second fit model, $CN_{Zn\text{-}Al} + CN_{Zn\text{-}Fe}$ was set to 3, and the other constrains left unchanged. The most significant difference with the previous try is a reduction of σ^2 from 0.015 to 0.009 Å^2, for a fit quality essentially comparable. Although data analysis is suggestive of a dioctahedral environment for Zn, it is impossible to be really conclusive with this technique alone, and independent confirmation by μ-XRD is warranted.

Table S2. Fit strategies for the simulations of P-EXAFS data.

	Zn-O	Zn-Al	Zn-Fe	Zn-Si
References				
Redhill, Fit 1 (δk = 2.6 - 11.5 Å^{-1}; δR = 1 - 3.4 Å)				
CN	x/6	x/3	-	x/4
R (Å)	f	f	-	f
σ^2 (Å^2)	f	f	-	f
ΔE_0 (eV)	c	c	-	c
Redhill, Fit 2 (δk = 2.6 - 11.5 Å^{-1}; δR = 1 - 3.4 Å)				
CN	x/6	x/3	-	x/4
R (Å)	f	f	-	x/80°
σ^2 (Å^2)	f	f	-	f
ΔE_0 (eV)	c	c	-	c
Soil samples				
Subsoil, Fit 1 (δk = 2.6 - 11.5 Å^{-1}; δR = 1 - 3.4 Å)				
CN	f	f	-	f
R (Å)	f	f	-	f
σ^2 (Å^2)	f	f	-	f
ΔE_0 (eV)	c	c	-	c
Subsoil, Fit 2 (δk = 2.6 - 11.5 Å^{-1}; δR = 1 - 3.4 Å)				
CN	x/6	x/3	-	x/4
R (Å)	f	f	-	f
σ^2 (Å^2)	f	f	-	f
ΔE_0 (eV)	c	c	-	c
Subsoil, Fit 3 (δk = 2.6 - 11.5 Å^{-1}; δR = 1 - 3.4 Å)				
CN	x/6	x/3	-	x/4
R (Å)	f	f	-	x/80° RH
σ^2 (Å^2)	f	f	-	f
ΔE_0 (eV)	c	c	-	c
Topsoil (δk = 2.6 - 10.5 Å^{-1}; δR = 1 - 3.4 Å)				
Trioctahedral hypothesis, Fit 1				
CN	x/6	c/6	c/6	f
R (Å)	f	x/RH	f	x/80° RH
σ^2 (Å^2)	f	c	c	x/RH
ΔE_0 (eV)	c	c	c	c
Topsoil (δk = 2.6 - 10.5 Å^{-1}; δR = 1 - 3.4 Å)				
Dioctahedral hypothesis, Fit 2				
CN	x/6	c/3	c/3	f
R (Å)	f	x/RH	f	x/80° Rh
σ^2 (Å^2)	f	c	c	x/RH
ΔE_0 (eV)	c	c	c	c

δk and δR are the intervals of the filtering windows used for the direct and inverse FTs.
CN, *R*, σ^2, ΔE_0: coordination number, interatomic distance, Debye-Waller factor, shift of the threshold energy.
CN at α = 10°, 55°, and 80° ($CN_{j,\alpha}$) was correlated to its value at α = 35° with formula (1) ;
x/6, x/3, x/4 = *CN* fixed at α = 35° to 6, 3, or 4; f = free parameters; c = correlated parameters;
x/80° = *R* fixed at its value at α = 80°, or at the value in Redhill (RH); x/RH = same value as in Redhill; c/6, c/3 = total *CN* for the shell fixed to 6 or 3.

Table S3. Results from the analysis of P-EXAFS data.

	Zn-O			Zn-Al			Zn-Fe			Zn-Si									
	CN	*R* (Å)	σ^2 (Å^2)	*CN*	*R* (Å)	σ^2 (Å^2)	*CN*	*R* (Å)	σ^2 (Å^2)	*CN*	*R* (Å)	σ^2 (Å^2)	ΔE_0 (eV)			correlations >0.25 between parameters			
Reference																			
Fit 1	**x/6**	**f**	**f**	**x/3**	**f**	**f**	-	-	-	**x/4**	**f**	**f**	**c**						
Redhill - α = 10°	6.3	2.04 (1)	0.008 (1)	4.4	2.98 (3)	0.013 (4)	-	-	-	1.9	3.21 (1)	0.010 (1)	1.9 (8)	N_i	53	ΔE_0 & R_Si	0.81	R_Si & R_Al	0.34
Redhill - α = 35°	6.0	2.04 (1)	0.008 (1)	3.0	2.98 (3)	0.013 (4)	-	-	-	4.0	3.21 (1)	0.010 (1)	1.9 (8)	# *f*	7	ΔE_0 & R_O	0.78	σ^2_Si & σ^2_Al	0.32
Redhill - α = 55°	5.7	2.04 (1)	0.008 (1)	1.5	2.98 (3)	0.013 (4)	-	-	-	6.3	3.21 (1)	0.010 (1)	1.9 (8)	reduced χ^2	5197	R_Si & R_O	0.63		
Redhill - α = 80°	5.4	2.04 (1)	0.008 (1)	0.1	2.98 (3)	0.013 (4)	-	-	-	8.4	3.21 (1)	0.010 (1)	1.9 (8)	R-factor	0.11	σ^2_Si & R_Al	-0.34		
Fit 2	**x/6**	**f**	**f**	**x/3**	**f**	**f**	-	-	-	**x/4**	**x/80°**	**f**	**c**						
Redhill - α = 10°	6.3	2.05 (1)	0.008 (1)	4.4	2.99 (3)	0.014 (5)	-	-	-	1.9	3.22	0.010 (1)	2.6 (5)	N_i	53	ΔE_0 & R_O	0.60		
Redhill - α = 35°	6.0	2.05 (1)	0.008 (1)	3.0	2.99 (3)	0.014 (5)	-	-	-	4.0	3.22	0.010 (1)	2.6 (5)	# *f*	6	σ^2_Si & σ^2_Al	0.28		
Redhill - α = 55°	5.7	2.05 (1)	0.008 (1)	1.5	2.99 (3)	0.014 (5)	-	-	-	6.3	3.22	0.010 (1)	2.6 (5)	reduced χ^2	5209				
Redhill - α = 80°	5.4	2.05 (1)	0.008 (1)	0.1	2.99 (3)	0.014 (5)	-	-	-	8.4	3.22	0.010 (1)	2.6 (5)	R-factor	0.10				
Soil samples																			
Subsoil																			
Fit 1	**f**	**f**	**f**	**f**	**f**	**f**	-	-	-	**f**	**f**	**f**	**c**						
subsoil - α = 10°	5.9 (5)	2.07 (1)	0.008 (1)	2.0 (8)	2.99 (2)	0.006 (6)	-	-	-	1.2 (5)	3.26 (1)	0.008 (2)	3.6 (9)	N_i	53	σ^2_Al & CN_Al	0.86	ΔE_0 & R_Si	0.74
subsoil - α = 35°	5.6 (5)	2.07 (1)	0.008 (1)	1.4 (8)	2.99 (2)	0.006 (6)	-	-	-	2.4 (5)	3.26 (1)	0.008 (2)	3.6 (9)	# *f*	10	σ^2_Si & CN_Si	0.86	R_Si & R_O	0.60
subsoil - α = 55°	5.3 (5)	2.07 (1)	0.008 (1)	0.7 (8)	2.99 (2)	0.006 (6)	-	-	-	3.9 (5)	3.26 (1)	0.008 (2)	3.6 (9)	reduced χ^2	3056	σ^2_O & CN_O	0.83	ΔE_0 & CN_Si	-0.34
subsoil - α = 80°	5.0 (5)	2.07 (1)	0.008 (1)	0.1 (8)	2.99 (2)	0.006 (6)	-	-	-	5.1 (5)	3.26 (1)	0.008 (2)	3.6 (9)	R-factor	0.07	ΔE_0 & R_O	0.82	σ^2_Si & R_Al	-0.30
Fit 2	**x/6**	**f**	**f**	**x/3**	**f**	**f**	-	-	-	**x/4**	**f**	**f**	**c**						
subsoil - α = 10°	6.3	2.06 (1)	0.009 (1)	4.4	2.98 (2)	0.012 (3)	-	-	-	1.9	3.24 (1)	0.013 (1)	2.3 (8)	N_i	53	ΔE_0 & R_O	0.80	R_Si & σ^2_Al	0.26
subsoil - α = 35°	6.0	2.06 (1)	0.009 (1)	3.0	2.98 (2)	0.012 (3)	-	-	-	4.0	3.24 (1)	0.013 (1)	2.3 (8)	# *f*	7	ΔE_0 & R_Si	0.78		
subsoil - α = 55°	5.7	2.06 (1)	0.009 (1)	1.5	2.98 (2)	0.012 (3)	-	-	-	6.3	3.24 (1)	0.013 (1)	2.3 (8)	reduced χ^2	3478	R_Si & R_O	0.61		
subsoil - α = 80°	5.4	2.06 (1)	0.009 (1)	0.1	2.98 (2)	0.012 (3)	-	-	-	8.4	3.24 (1)	0.013 (1)	2.3 (8)	R-factor	0.09	R_Si & R_Al	0.35		
Fit 3	**x/6**	**f**	**f**	**x/3**	**f**	**f**	-	-	-	**x/4**	**x/80°RH**	**f**	**c**						
subsoil - α = 10°	6.3	2.05 (1)	0.009 (1)	4.4	2.97 (2)	0.011 (3)	-	-	-	1.9	3.22	0.013 (1)	1.1 (5)	N_i	53	ΔE_0 & R_O	0.65		
subsoil - α = 35°	6.0	2.05 (1)	0.009 (1)	3.0	2.97 (2)	0.011 (3)	-	-	-	4.0	3.22	0.013 (1)	1.1 (5)	# *f*	6				
subsoil - α = 55°	5.7	2.05 (1)	0.009 (1)	1.5	2.97 (2)	0.011 (3)	-	-	-	6.3	3.22	0.013 (1)	1.1 (5)	reduced χ^2	3683				
subsoil - α = 80°	5.4	2.05 (1)	0.009 (1)	0.1	2.97 (2)	0.011 (3)	-	-	-	8.4	3.22	0.013 (1)	1.1 (5)	R-factor	0.10				
Topsoil																			
Fit 1	**x/6**	**f**	**f**	**c/6**	**x/RH**	**c**	**c/6**	**f**	**c**	**f**	**x/80°RH**	**x/RH**	**c**						
topsoil - α = 10°	6.3	2.05 (1)	0.009 (1)	4.3 (5)	2.99	0.015 (2)	4.3 (5)	3.08 (2)	0.015 (2)	1.2 (3)	3.22	0.010	1.7 (8)	N_i	47	CN_Fe &	-0.95	R_Fe &	-0.58
topsoil - α = 35°	6.0	2.05 (1)	0.009 (1)	2.9 (5)	2.99	0.015 (2)	3.0 (5)	3.08 (2)	0.015 (2)	2.5 (3)	3.22	0.010	1.7 (8)	# *f*	7	ΔE_0 & delR_O	0.75	R_Fe &	0.58
topsoil - α = 55°	5.7	2.05 (1)	0.009 (1)	1.5 (5)	2.99	0.015 (2)	1.5 (5)	3.08 (2)	0.015 (2)	4.0 (3)	3.22	0.010	1.7 (8)	reduced χ^2	10595	σ^2 & R_Fe	0.63	σ^2 & CN_Al	-0.57
topsoil - α = 80°	5.4	2.05 (1)	0.009 (1)	0.1 (5)	2.99	0.015 (2)	0.1 (5)	3.08 (2)	0.015 (2)	5.3 (3)	3.22	0.010	1.7 (8)	R-factor	0.09	σ^2 & CN_Fe	0.61	ΔE_0 & R_Fe	0.36
																		R_Fe & R_O	0.26
Fit 2	**x/6**	**f**	**f**	**c/3**	**x/RH**	**c**	**c/3**	**f**	**c**	**f**	**x/80°RH**	**x/RH**	**c**						
topsoil - α = 10°	6.3	2.05 (1)	0.010 (1)	2.0 (4)	2.99	0.009 (2)	2.3 (4)	3.10 (1)	0.009 (2)	1.2 (3)	3.22	0.010	2.0 (7)	N_i	47	σ^2 & CN_Fe	0.81	ΔE_0 & R_Fe	0.35
topsoil - α = 35°	6.0	2.05 (1)	0.010 (1)	1.4 (4)	2.99	0.009 (2)	1.6 (4)	3.10 (1)	0.009 (2)	2.5 (3)	3.22	0.010	2.0 (7)	# *f*	7	ΔE_0 & R_O	0.75	σ^2 & R_Fe	0.33
topsoil - α = 55°	5.7	2.05 (1)	0.010 (1)	0.7 (4)	2.99	0.009 (2)	0.8 (4)	3.10 (1)	0.009 (2)	3.9 (3)	3.22	0.010	2.0 (7)	reduced χ^2	7326	R_Fe & CN_Al	-0.48	R_Fe & R_O	0.27
topsoil - α = 80°	5.4	2.05 (1)	0.010 (1)	0.1 (4)	2.99	0.009 (2)	0.1 (4)	3.10 (1)	0.009 (2)	5.2 (3)	3.22	0.010	2.0 (7)	R-factor	0.07	R_Fe &	0.41	ΔE_0 & CN_Si	-0.26

N_{idp} = number of independent parameters; # *f* = number of adjusted parameters. Precisions are shown in brackets (1 std). S_0^2 was fixed to 0.85. For further abbreviations see Table S2.

2.4. Laboratory X-ray diffraction

The mineralogy of the clay fractions from the three soils was characterized also in the laboratory with a Bruker D5000 diffractometer equipped with a Cu anode and a Si(Li)-solid-state detector. A step interval of 0.04° 2θ and a counting time of 12 seconds per step were used. The 00l reflections were measured on oriented aggregates prepared by air-drying clay suspensions onto glass slides. The clays were Na-saturated and afterwards treated with ethylene glycol. Trioctahedral chlorite and dioctahedral clays, including kaolinite, illite, mica, smectites and interstratified illite-smectite, were identified in all samples (Figure S11).

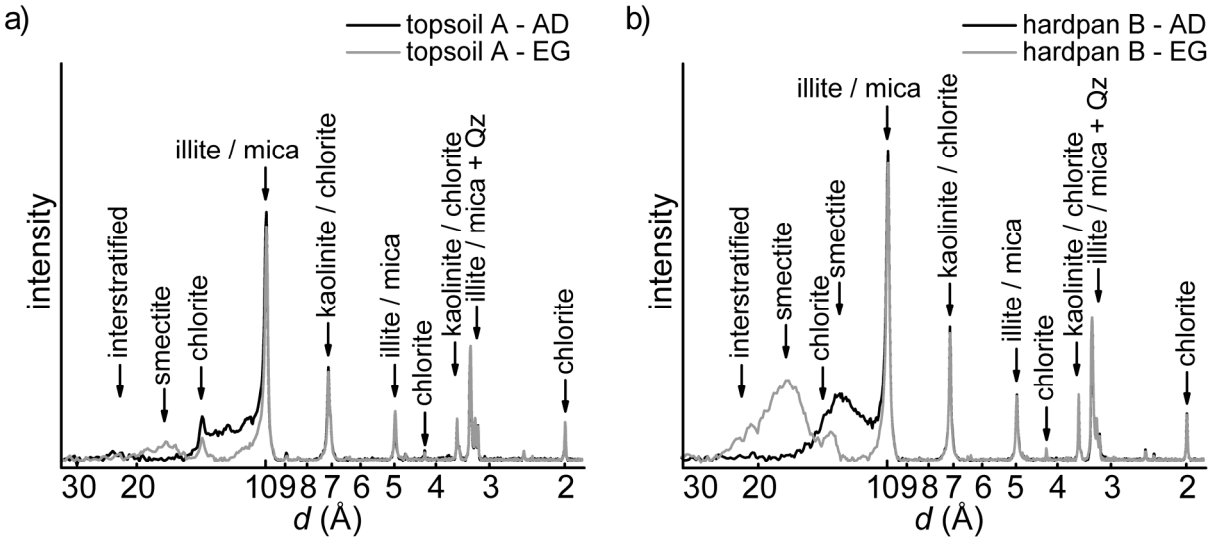

Figure S11. XRD trace of 00l reflections from the <2µm clay fraction in *d*-spacing (Å) from the topsoil (sample Aa) and the subsoil or hardpan (sample Bb). AD: air dried; EG: ethylene glycol; Qz: quartz.

Literature Cited

(1) Laird, D. A.; Dowdy, R. H.; Munter, R. C. Suspension nebulization analysis of clays by inductively coupled plasma-atomic emission spectroscopy. *Soil Sci. Soc. Am. J.* **1991,** *55*, 274-278.

(2) Mehra, O. P.; Jackson, M. L. Iron oxide removal from soils and clays by a dithionite-citrate system buffered with sodium bicarbonate. *Clays Clay Mineral.* **1960,** *7*, 313–317.

(3) Jacquat, O.; Voegelin, A.; Villard, A.; Marcus, M. A.; Kretzschmar, R. Formation of Zn-rich phyllosilicate, Zn-layered double hydroxide and hydrozincite in contaminated calcareous soils. *Geochim. Cosmochim. Acta* **2008,** *72*, 5037-5054.

(4) Nachtegaal, M.; Marcus, M. A.; Sonke, J. E.; Vangronsveld, J.; Livi, K.; van der Lelie, D.; Sparks, D. L. Effects of in situ remediation on the speciation and bioavailability of zinc in a smelter contaminated soil. *Geochim. Cosmochim. Acta* **2005,** *69*, 4649-4664.

(5) Panfili, F.; Manceau, A.; Sarret, G.; Spadini, L.; Kirpichtchikova, T.; Bert, V.; Laboudigue, A.; Marcus, M. A.; Ahamdach, N.; Libert, M. F. The effect of phytostabilization on Zn speciation in a dredged contaminated sediment using scanning electron microscopy, X-ray fluorescence, EXAFS spectroscopy and principal components analysis. *Geochim. Cosmochim. Acta* **2005,** *69*, 2265-2284.

(6) Voegelin, A.; Pfister, S.; Scheinost, A. C.; Marcus, M. A.; Kretzschmar, R. Changes in zinc speciation in field soil after contamination with zinc oxide. *Environ. Sci. Technol.* **2005,** *39*, 6616-6623.

(7) Newville, M. IFFEFFIT: interactive XAFS analysis and FEFF fitting. *J. Synch. Rad.* **2001,** *8*, 322-324.
(8) Ravel, B.; Newville, M. ATHENA, ARTEMIS, HEPHAESTUS: data analysis for X-ray absorption spectroscopy using IFEFFIT. *J. Synch. Rad.* **2005,** *12*, 537-541.
(9) Rehr, J. J.; Mustre de Leon, J.; Zabinsky, S. I.; Albers, R. C. Theoretical X-ray absorption fine structure standards. *J. Am. Chem. Soc.* **1991,** *113*, 5135-5145.
(10) O'Day, P. A.; Rehr, J. J.; Zabinsky, S. I.; Brown, G. E., Jr. Extended X-ray absorption fine structure (EXAFS) analysis of disorder and multiple-scattering in complex crystalline solids. *J. Am. Chem. Soc.* **1994,** *116*, 2938-2949.
(11) Manceau, A.; Chateigner, D.; Gates, W. P. Polarized EXAFS, distance-valence least-squares modeling (DVLS) and quantitative texture analysis approaches to the structural refinement of Garfield nontronite. *Phys. Chem. Mineral.* **1998,** *25*, 347-365.
(12) Schlegel, M.; Manceau, A.; Chateigner, D.; Charlet, L. Sorption of metal ions on clay minerals. I. Polarized EXAFS evidence for the adsorption of Co on the edges of hectorite particles. *J. Coll. Interf. Sci.* **1999,** *215*, 140-158.
(13) Manceau, A.; Bonnin, D.; Stone, W. E. E.; Sanz, J. Distribution of Fe in the octahedral sheet of trioctahedral micas by polarized EXAFS. Comparison with NMR results. *Phys. Chem. Mineral.* **1990,** *17*, 363-370.
(14) Schlegel, M. L.; Manceau, A.; Charlet, L.; Hazemann, J. L. Adsorption mechanism of Zn on hectorite as a function of time, pH, and ionic strength. *Am. J. Sci.* **2001,** *301*, 798-830.
(15) Stern, E. A. Number of relevant independent points in x-ray-absorption fine-structure spectra. *Phys. Rev.* **1993,** *B48*, 9825-9827.
(16) Voegelin, A.; Scheinost, A. C.; al., e. Slow formation and dissolution of Zn precipitates in soil: A combined column-transport and XAFS study. *Environ. Sci. Technol.* **2002,** *36*, 3749-3754.
(17) Ford, R. G.; Sparks, D. L. The nature of Zn precipitates formed in the presence of pyrophyllite. *Environ. Sci. Technol.* **2000,** *34*, 2479–2483.
(18) Scheinost, A. C.; Kretzschmar, R.; Pfister, S.; Roberts, D. R. Combining selective sequential extractions, X-ray absorption spectroscopy and principal component analysis for quantitative zinc speciation in soil. *Environ. Sci. Technol.* **2002,** *36*, 5021-5028.
(19) Schlegel, M. L.; Manceau, A. Evidence for the nucleation and epitaxial growth of Zn phyllosilicate on montmorillonite. *Geochim. Cosmochim. Acta* **2006,** *70*, 901-917.
(20) Schlegel, M. L.; Manceau, A.; Charlet, L.; Chateigner, D.; Hazemann, J. L. Sorption of metal ions on clay minerals. III. Nucleation and epitaxial growth of Zn phyllosilicate on the edges of hectorite. *Geochim. Cosmochim. Acta* **2001,** *65*, i4155-4170.
(21) Manceau, A.; Lanson, B.; Schlegel, M. L.; Hargé, J. C.; Musso, M.; Eybert-Bérard, L.; Hazemann, J. L.; Chateigner, D.; Lamble, G. M. Quantitative Zn speciation in smelter-contaminated soils by EXAFS spectroscopy. *Am. J. Sci.* **2000,** *300*, 289-343.
(22) Teo, B. K., *EXAFS: basic principles and data analysis*. Springer-Verlag: Berlin, 1986; p 349.
(23) Koningsberger, D. C.; Prins, R., *X-ray Absorption. Principles, Applications, Techniques of EXAFS, SEXAFS and XANES*. John Wiley & Sons: New York, 1988; p 673.
(24) Manceau, A.; Tommaseo, C.; Rihs, S.; Geoffroy, N.; Chateigner, D.; Schlegel, M.; Tisserand, D.; Marcus, M. A.; Tamura, N.; Chen, Z. S. Natural speciation of Mn, Ni and Zn at the micrometer scale in a clayey paddy soil using X-ray fluorescence, absorption, and diffraction. *Geochim. Cosmochim. Acta* **2005,** *69*, 4007-4034.